

The ATLAS^{3D} project – V. The CO Tully–Fisher relation of early-type galaxies

Timothy A. Davis,^{1*} Martin Bureau,¹ Lisa M. Young,^{2,†} Katherine Alatalo,³ Leo Blitz,³ Michele Cappellari,¹ Nicholas Scott,¹ Maxime Bois,^{4,5} Frédéric Bournaud,⁶ Roger L. Davies,¹ P. Tim de Zeeuw,^{4,7} Eric Emsellem,^{4,5} Sadegh Khochfar,⁸ Davor Krajnović,⁴ Harald Kuntschner,⁹ Pierre-Yves Lablanche,⁵ Richard M. McDermid,¹⁰ Raffaella Morganti,^{11,12} Thorsten Naab,¹³ Tom Oosterloo,^{11,12} Marc Sarzi,¹⁴ Paolo Serra¹¹ and Anne-Marie Weijmans^{15,‡}

¹Sub-department of Astrophysics, University of Oxford, Denys Wilkinson Building, Keble Road, Oxford OX1 3RH

²Physics Department, New Mexico Institute of Mining and Technology, Socorro, NM 87801, USA

³Department of Astronomy, Campbell Hall, University of California, Berkeley, CA 94720, USA

⁴European Southern Observatory, Karl-Schwarzschild-Strasse 2, 85748 Garching, Germany

⁵Université Lyon 1, Observatoire de Lyon, Centre de Recherche Astrophysique de Lyon and Ecole Nationale Supérieure de Lyon, 9 avenue Charles André, F-69230 Saint-Genis Laval, France

⁶Laboratoire AIM Paris-Saclay, CEA/IRFU/Sap CNRS Université Paris Diderot, 91191 Gif-sur-Yvette Cedex, France

⁷Sterrewacht Leiden, Leiden University, Postbus 9513, 2300 RA Leiden, the Netherlands

⁸Max-Planck-Institut für extraterrestrische Physik, PO Box 1312, D-85478 Garching, Germany

⁹Space Telescope European Coordinating Facility, European Southern Observatory, Karl-Schwarzschild-Strasse 2, 85748 Garching, Germany

¹⁰Gemini Observatory, Northern Operations Center, 670 N. A'ohoku Place, Hilo, HI 96720, USA

¹¹Netherlands Institute for Radio Astronomy (ASTRON), Postbus 2, 7990 AA Dwingeloo, the Netherlands

¹²Kapteyn Astronomical Institute, University of Groningen, Postbus 800, 9700 AV Groningen, the Netherlands

¹³Max-Planck-Institut für Astrophysik, Karl-Schwarzschild-Strasse 1, 85741 Garching, Germany

¹⁴Centre for Astrophysics Research, University of Hertfordshire, Hatfield, Herts AL1 9AB

¹⁵Dunlap Institute for Astronomy & Astrophysics, University of Toronto, 50 St George Street, Toronto, ON M5S 3H4, Canada

Accepted 2011 January 2. Received 2010 December 27; in original form 2010 November 2

ABSTRACT

We demonstrate here using both single-dish and interferometric observations that CO molecules are an excellent kinematic tracer, even in high-mass galaxies, allowing us to investigate for the first time the CO Tully–Fisher relation (CO-TFR) of early-type galaxies. We compare the TFRs produced using both single-dish and interferometric data and various inclination estimation methods, and evaluate the use of the velocity profile shape as a criterion for selecting galaxies in which the molecular gas extends beyond the peak of the rotation curve. We show that the gradient and zero-point of the best-fitting relations are robust, independent of the velocity measure and inclination used, and agree with those of relations derived using stellar kinematics. We also show that the early-type CO-TFR is offset from the CO-TFR of spirals by 0.98 ± 0.22 mag at K_s band, in line with other results. The intrinsic scatter of the relation is found to be ≈ 0.4 mag, similar to the level found in the spiral galaxy population. Next-generation facilities such as the Large Millimeter Telescope and the Atacama Large Millimeter/Sub-millimeter Array should allow this technique to be used in higher redshift systems, providing a simple new tool to trace the mass-to-light ratio evolution of the most massive galaxies over cosmic time.

Key words: ISM: kinematics and dynamics – galaxies: elliptical and lenticular, cD – galaxies: evolution – galaxies: kinematics and dynamics – galaxies: spiral – galaxies: structure.

*E-mail: timothy.davis@astro.ox.ac.uk

†Adjunct Astronomer with the National Radio Astronomy Observatory.

‡Dunlap Fellow.

1 INTRODUCTION

The Tully–Fisher relation (TFR; Tully & Fisher 1977) of spiral galaxies has proved itself to be one of the most important correlations in extragalactic astrophysics. For example, its use as a distance measure is vital in extending the cosmic distance ladder, allowing the scale of structures in the nearby Universe to be determined and studied. The underlying cause of this relation between the luminosity and rotational velocity is usually interpreted as the product of a relatively constant total (luminous plus dark) mass-to-light ratio (M/L) in the local spiral galaxy population (Gavazzi 1993; Zwaan et al. 1995), and hence a strong coupling between the dark and luminous masses. Studying the slope and zero-point of the TFR is thus also a powerful probe of the M/L evolution of galaxies (e.g. Phillipps 1989; Sprayberry et al. 1995; Bell & de Jong 2001).

The TFR as introduced by Tully & Fisher (1977) uses rotational velocities derived from H I linewidths in spiral galaxies, which should approximate the true projected circular velocity of the galaxies as long as the H I distributions are relaxed and reach into the flat parts of the galaxy rotation curves. Over the years, however, the TFR has gradually been recognized as denoting the empirical relationship between the luminosity and rotation velocity of galaxies (generally disc galaxies) as measured with a variety of kinematic tracers, using differing techniques at various wavelengths.

Studying the TFR in lenticular (S0) and elliptical (E) galaxies [collectively referred to as early-type galaxies (ETGs)] is problematic, as they do not all possess extended relaxed atomic gas distributions. Indeed, it has been shown that even where H I is present in ETGs it can be disturbed and hence the measured linewidths are in some cases unrelated to galaxy properties (e.g. Morganti et al. 2006; Williams, Bureau & Cappellari 2010). Although widespread, the ionized gas is generally faint, with significant pressure support, and is thus not ideal either (Bertola et al. 1995). The TFR of ETGs is nevertheless important, as these galaxies are believed to have turbulent formation histories and the TFR may give clues about their assembly and evolution. For example, many authors have suggested that S0 galaxies have avoided violent interactions and are the faded descendants of high-redshift spirals (e.g. Dressler 1980; Dressler et al. 1997). In this scenario, galaxies become dimmer whilst keeping the same dynamical mass, leading to an offset TFR.

Due to the problems listed above, stellar tracers of the galactic rotation are generally used in ETGs. Due to the importance of the pressure support in these systems, however, stellar dynamical modelling or an asymmetric drift correction is required to extract the true circular velocities. This adds additional systematic uncertainties to the already challenging stellar kinematic observations (which must reach sufficiently large radii). Recent analyses of ETGs have suggested that galaxies do indeed have a measurable offset from the spiral TFR, of around 0.5–1.0 mag at K band (Neistein et al. 1999; Bedregal, Aragón-Salamanca & Merrifield 2006; Williams et al. 2010). Magorrian & Ballantyne (2001), Gerhard et al. (2001) and Rijcke et al. (2007) have all considered extending this approach to construct TFRs that include E galaxies and find that these are also offset from the spiral TFR, by 0.5–1.5 mag at optical wavelengths.

In this work, we consider the use of carbon monoxide (CO) as a tracer of the circular velocity, of fast-rotating ETGs. CO is thought to be free of many of the problems that beset H I in early types. As part of the ATLAS^{3D} survey of ETGs (Cappellari et al. 2011, hereinafter Paper I), we have found that the molecular gas is reasonably abundant in ETGs (Young et al. 2011, hereinafter Paper IV), with

≈22 per cent of ETGs in the local volume (<42 Mpc distant) containing a substantial molecular gas reservoir. The detection rate of the molecular gas is also independent of the galaxy luminosity and mass (the two most important TFR parameters), providing a direct and unbiased probe of the potential in high-mass galaxies, which are often H I poor (Serra et al., in preparation). The molecular gas is likely to be relaxed in most galaxies under study, even in clusters where H I may be undergoing ram-pressure stripping (Toribio & Solanes 2009), due to the short dynamical time-scales in the central parts of the galaxies, where it is usually found (e.g. Wrobel & Kenney 1992; Young 2002; Crocker et al. 2008, 2009, 2011; Young, Bureau & Cappellari 2008). Therefore, CO provides a powerful, directly observable measure of the circular velocity of galaxies of all masses and morphological types, irrespective of the environment. Additionally, the small beamsizes of the mm-wave single-dish telescopes used to detect CO eliminate source confusion, at least in nearby galaxies, while current interferometers routinely yield arc-second angular resolutions.

The possibility of using CO linewidths to investigate the TFR was first explored by Dickey & Kazes (1992) and this method has since been used by various authors to investigate the CO-TFR of spiral and irregular galaxies (e.g. Schoeniger & Sofue 1994, 1997; Tutui & Sofue 1997; Lavezzi & Dickey 1998; Tutui et al. 2001) and quasars (Ho 2007). In spiral galaxies, the CO velocity widths obtained are directly comparable to those found in H I (Lavezzi 1997). Young et al. (2008) have also demonstrated that CO is a good tracer of the circular velocity in a small sample of ETGs, from a comparison with detailed dynamical modelling of the stellar kinematics, but this has yet to be demonstrated for a larger sample.

One possible complication introduced when using CO as a dynamical tracer is that the molecular gas in early types is usually confined to the inner regions. This means that we are only able to probe the kinematics where the dark matter does not yet play a significant role. This is the opposite of H I TF analyses, which are generally probing H I at large radii, in the dark matter dominated part of the rotation curve. As such, a TFR measured in the central region could be considered more similar to the Faber–Jackson (central velocity dispersion–luminosity) relation (Faber & Jackson 1976). The ETG CO-TFR will therefore only be directly comparable to TF results from H I if the ‘disc–halo conspiracy’, where the dark matter flattens the rotation curve at a similar velocity to that found (from the luminous material) in the inner regions, also holds for ETGs (Kent 1987; Sancisi 2004; Gavazzi et al. 2007).

Some authors have suggested that there is a change in the slope of the TFR for high-mass disc galaxies, brighter than an absolute K -band magnitude of ≈ -23.75 (Peletier & Willner 1993; Verheijen 2001; Noordermeer & Verheijen 2007). A break in the TFR at a similar position is also found for E galaxies (Gerhard et al. 2001; Rijcke et al. 2007). It has been suggested that this break occurs because many massive galaxies have declining circular velocity profiles, whereas low-mass galaxies have relatively flat circular velocity curves. In other words, the aforementioned disc–halo conspiracy is not perfect in ETGs and many have a local rotation velocity peak at small radii. The radius where one measures the velocity hence becomes important (see Noordermeer & Verheijen 2007). Measures of the maximal rotation produce a much larger break than measures of the asymptotic rotation velocity, supporting this interpretation. Clearly, the existence of a break in the TFR could lead to systematic biases when deriving distances or probing the galaxy evolution. Fortunately, however, we show in this paper that our CO velocities are consistent with measures of the rotation beyond the peak of the galaxy circular velocity curves.

This work, to the best of the author’s knowledge, represents the first attempt to create a CO-TFR for ETGs. One can identify two major pitfalls that need to be overcome for this approach to be successful. First, as discussed above, it has been shown that the CO in ETGs is often very centrally concentrated and hence in some galaxies it may not reach beyond the peak of the rotation curve. Identifying such cases is critical to obtain a useful TFR. Secondly, it has been shown that the molecular gas in ETGs is often misaligned with respect to the stars (e.g. Schinnerer & Scoville 2002; Young 2002; Crocker et al. 2008, 2009; Young et al. 2008). In these cases, the inclination of the stars is not useful and we require an estimate of the inclination of the molecular gas itself in order to deproject its observed rotation velocity.

Our goal in this paper is therefore to explore and demonstrate that, despite the potential pitfalls highlighted above, ETGs do appear to follow a robust luminosity–rotational velocity relation, consistent with that measured using other tracers at the same radii. Although technical aspects will certainly be improved and the interpretation of this relation remains uncertain, an ETG CO-TFR is a tantalizing and promising tool for galaxy evolution studies, worthy of further consideration. In Section 2 of this paper, we discuss the data used in this work, outlining the observations in Sections 2.3 and 2.4, the methods for estimating the inclination in Section 2.5 and our method for extracting the circular velocity from observed CO linewidths in Section 2.6. In Section 3, we compare these velocities with other measures, such as circular velocities derived from dynamical models, and show that it is possible to use simple criteria to select galaxies where CO is a good tracer of the circular velocity beyond the peak of the galaxy rotation curve. In Section 4, we present our ETG CO-TFRs and explore how different data and inclination estimates affect the resulting relations. In Section 5, we more fully discuss our results and compare them with previous TFR results derived using other tracers. We summarize our conclusions in Section 6.

2 DATA

2.1 Sample

The sample used here is comprised of the galaxies detected in the CO(1–0) emission in Paper IV. The CO(1–0) and (2–1) emissions were observed in all galaxies from the complete, volume-limited ATLAS^{3D} sample of 260 S0 and E galaxies (see Paper I for full details). Upper limits for non-detections are typically in the range 10^7 – $10^8 M_{\odot}$, depending on the distance, assuming a standard CO-to-H₂ conversion factor. The detected galaxies used here range in molecular gas masses from 10^7 to $10^9 M_{\odot}$, with molecular gas mass fractions between 10^{-4} and $10^{-1} M_{\odot}/L_{K_s}$, where L_{K_s} is the K_s -band luminosity from the Two-Micron All-Sky Survey (2MASS) (Jarrett et al. 2000; Skrutskie et al. 2006). Only fast-rotating galaxies were detected.

Of the 52 detections by Paper IV, four are detected only in CO(2–1) and a further eight had an insufficient signal-to-noise ratio to perform the analysis required here, leaving 40. In addition to these, we include the ETGs IC 2099, NGC 4292 and 4309, which were detected in CO as part of the initial ATLAS^{3D} survey, but were later removed from the sample because they are too faint at the K_s band to meet the final sample selection criteria. This should not affect the TFR. This leaves a total of 43 galaxies, the properties of which are listed in Table 1.

2.2 Photometric data

The K -band magnitudes used in this paper are $K_{s,\text{total}}$ from the 2MASS (Jarrett et al. 2000; Skrutskie et al. 2006). These $K_{s,\text{total}}$ magnitudes are measured over large apertures to include the total flux from the galaxy using the techniques developed in Kron (1980) and curves of growth (see Jarrett et al. 2000 for further details). They have been widely used in the astronomical community and are found to be robust to ≈ 0.1 mag (Noordermeer & Verheijen 2007).

2.3 CO single-dish data

As reported in Paper IV, the Institut de Radioastronomie Millimétrique (IRAM) 30-m telescope at Pico Veleta, Spain, was used for simultaneous observations of CO(1–0) and CO(2–1) in our galaxies. The primary beam full width at half-maximum (FWHM) is 23 and 12 arcsec for CO(1–0) and CO(2–1), respectively. The filterbank back-end gave an effective total bandwidth of 512 MHz (≈ 1330 km s^{−1}) and a raw spectral resolution of 1 MHz (2.6 km s^{−1}) for CO(1–0). The system temperatures ranged from 190 to 420 K for CO(1–0). The time on source was interactively adjusted so that the final, co-added CO(1–0) spectrum for each galaxy had a rms noise level of ≈ 3.0 mK T_{a}^* (≈ 19 mJy) per binned 31 km s^{−1} channel. For further details, see Paper IV.

The CO(1–0) and CO(2–1) spectra for each detected galaxy, binned to 31 km s^{−1} channels, were analysed to find the velocities at which the flux drops to 20 per cent of the peak height. Each spectrum was read into a routine which, working outwards from the galaxy systemic velocity, locates the first channel where the velocity drops to 20 per cent of the peak value. The measurements were inspected by eye to ensure noise peaks and troughs were not affecting the result. This is analogous to the method used by Tully & Fisher (1977) for measuring H I linewidths. The resulting velocity width is henceforth denoted by W_{20} . If the molecular gas is a good tracer of the circular velocity in our galaxies, then the linewidth should approximate twice the projected rotational velocity, if the molecular gas distribution reaches beyond the peak of the galaxy rotation curve (Dickey & Kazes 1992).

Fig. 1 shows a comparison between W_{20} linewidths measured from CO(1–0) and CO(2–1) spectra. One might expect it to be easier to measure linewidths using CO(2–1), as Paper IV has shown that this transition is usually one to four times brighter than CO(1–0) (due to the beam dilution and/or intrinsic effects), but Fig. 1 shows that the agreement between the two measurements is generally good. However, almost all the scatter is below the 1:1 line. In these cases, the molecular gas likely extends farther than the ≈ 12 arcsec FWHM of the CO(2–1) beam and the CO(2–1) linewidth measurements are systematically biased low. In Section 4.1.3, we in fact show that in some cases even the ≈ 23 arcsec CO(1–0) beam is not extended enough to retrieve the full velocity width. The number of galaxies for which this is a concern is small, however, and in the rest of this paper we will therefore use linewidths measured from the CO(1–0) spectra.

The instrumental dispersion is small compared to our 31 km s^{−1} channels, so we did not correct the linewidths for it. We also chose not to use corrections for the turbulence or line-broadening, as these are generally derived through a comparison with H I linewidths in spirals (Tully & Fouque 1985; Lavezzi & Dickey 1998; Tutui & Sofue 1999) and hence may not be applicable to ETGs. The velocity dispersion in the gas is expected to be small (e.g. Okuda et al. 2005). In Section 3.1, we attempt to quantify any biases introduced by ignoring these corrections. The derived W_{20} velocity widths are

Table 1. Parameters of the ATLAS^{3D} early-type CO-rich galaxies used in this paper.

Galaxy	T -type	$W_{20,SD}$ (km s ⁻¹)	$W_{20,inter}$ (km s ⁻¹)	$i_{b/a}$ (°)	i_{dust} (°)	$i_{tilted-ring}$ (°)	i_{best} (°)	M_{K_s} (mag)	Dhorn (SD)	Dhorn (best)	Telescope	Reference
(1)	(2)	(3)	(4)	(5)	(6)	(7)	(8)	(9)	(10)	(11)	(12)	(13)
IC 0676	-1.3	93	170	58 ± 3	–	69 ± 6	69 ± 6	-22.20	–	–	C	1
IC 0719	-2.0	343	353	82 ± 1	79 ± 1	74 ± 5	74 ± 5	-22.70	x	x	C	1
IC 1024	-2.0	221	240	79 ± 1	72 ± 1	–	72 ± 1	-21.70	x	x	C	–
*IC 2099	-1.5	93	–	83 ± 1	–	–	83 ± 1	-21.40	?	?	–	–
NGC 0524	-1.2	312	320	28 ± 8	19 ± 7	44 ± 28	19 ± 7	-24.70	x	x	P	2
NGC 1222	-3.0	156	210	41 ± 5	41 ± 3	–	41 ± 3	-22.70	?	–	C	1
NGC 1266	-2.1	187	180	47 ± 4	26 ± 5	–	26 ± 5	-22.90	–	–	C	1
NGC 2685	-1.0	156	220	70 ± 1	61 ± 1	70 ± 10	61 ± 1	-22.80	–	–	O	4
NGC 2764	-2.0	312	310	65 ± 2	65 ± 1	76 ± 15	65 ± 1	-23.20	x	x	C	1
NGC 2768	-4.4	322	360	36 ± 6	–	–	36 ± 6	-24.70	x	x	P	2
NGC 2824	-2.0	312	310	56 ± 3	61 ± 1	–	61 ± 1	-22.90	x	x	C	1
NGC 3032	-1.9	143	150	36 ± 6	35 ± 3	46 ± 11	35 ± 3	-22.00	x	x	B	3
NGC 3182	0.4	218	–	39 ± 5	35 ± 3	–	35 ± 3	-23.20	x	x	–	–
NGC 3489	-1.2	292	240	62 ± 2	–	56 ± 15	62 ± 2	-23.00	?	x	P	2
NGC 3619	-0.9	405	–	44 ± 4	48 ± 2	–	48 ± 2	-23.50	x	x	–	–
NGC 3626	-1.0	374	374	51 ± 3	61 ± 2	67 ± 5	67 ± 5	-23.30	x	x	C	1
NGC 3665	-2.1	624	630	90 ± 1	64 ± 1	74 ± 35	64 ± 1	-24.90	x	x	C	1
NGC 4119	-1.3	156	170	83 ± 1	67 ± 1	69 ± 3	69 ± 3	-22.60	?	–	C	1
NGC 4150	-2.1	234	238	50 ± 3	54 ± 2	54 ± 3	54 ± 3	-21.60	x	x	B	3
*NGC 4292	-1.7	187	190	49 ± 3	50 ± 2	46 ± 14	50 ± 2	-21.54	?	x	C	1
*NGC 4309	-1.5	124	–	69 ± 2	61 ± 1	–	61 ± 1	-20.91	–	–	–	–
NGC 4324	-0.9	218	360	73 ± 1	64 ± 1	62 ± 1	62 ± 1	-22.60	?	x	C	1
NGC 4429	-1.1	499	532	68 ± 2	68 ± 1	60 ± 16	68 ± 1	-24.30	x	x	C	1
NGC 4435	-2.1	405	380	48 ± 4	52 ± 2	–	52 ± 2	-23.80	x	x	C	1
NGC 4459	-1.4	391	400	43 ± 4	46 ± 2	47 ± 2	47 ± 2	-23.90	x	x	B	3
NGC 4477	-1.9	204	260	36 ± 6	26 ± 5	38 ± 3	38 ± 3	-23.70	?	x	P	2
NGC 4526	-1.9	655	663	82 ± 1	78 ± 1	64 ± 8	82 ± 1	-24.60	x	x	B	3
NGC 4684	-1.2	249	–	77 ± 1	–	–	77 ± 1	-22.20	?	?	–	–
NGC 4694	-2.0	93	65	69 ± 2	–	–	69 ± 2	-22.10	–	–	C	1
NGC 4710	-0.9	312	430	78 ± 1	88 ± 1	86 ± 6	86 ± 6	-23.50	x	x	C	1
NGC 4753	-1.4	530	–	61 ± 2	75 ± 1	–	75 ± 1	-25.10	x	x	–	5
NGC 5173	-4.9	187	–	24 ± 9	–	–	24 ± 9	-22.90	x	x	–	–
NGC 5273	-1.9	218	–	38 ± 5	38 ± 3	–	38 ± 3	-22.40	x	x	–	–
NGC 5379	-2.0	124	120	80 ± 1	64 ± 1	–	64 ± 1	-22.10	–	–	C	1
NGC 6014	-1.9	156	160	29 ± 7	22 ± 6	22 ± 10	22 ± 6	-23.00	x	x	C	1
NGC 7465	-1.9	158	180	56 ± 3	70 ± 1	58 ± 9	70 ± 1	-22.80	x	–	C	1
PGC 29321	0.0	124	–	31 ± 7	38 ± 3	–	38 ± 3	-21.60	–	–	–	–
PGC 56772	-2.0	249	–	64 ± 2	57 ± 2	–	57 ± 2	-22.00	?	?	–	–
PGC 58114	-2.0	202	240	71 ± 1	–	76 ± 30	71 ± 1	-21.60	–	x	C	1
PGC 61468	0.0	218	–	51 ± 3	–	–	51 ± 3	-21.60	?	?	–	–
UGC 05408	-3.3	156	–	31 ± 7	–	–	31 ± 7	-21.90	x	x	–	–
UGC 06176	-2.0	249	230	70 ± 2	68 ± 1	–	68 ± 1	-22.60	?	–	C	1
UGC 09519	-1.9	187	210	47 ± 4	41 ± 3	63 ± 7	41 ± 3	-22.10	?	x	C	1

Notes. Column (1) lists the galaxy name. Galaxies with stars (*) next to their name are early types that were observed by Paper IV but are not included in the ATLAS^{3D} sample. Column (2) contains the morphological T type from the HyperLeda data base (Paturel et al. 2003). This morphology indicator was not used for the sample selection (see Paper I). Columns (3) and (4) list the velocity widths at 20 per cent of the peak flux, derived from single-dish and interferometric data, respectively. The error in these quantities was estimated as half the velocity width of an individual channel, 15 km s⁻¹. Column (5) contains the inclination derived from galaxy axial ratios. The quoted errors only take into account the error in the measurement of the optical axial ratio, as reported in the NED. Column (6) contains the inclination derived from the ellipse fitting to unsharp-masked dust images. The error is estimated to be 5 per cent on the measurement of both the minor and the major axes. Column (7) contains the inclinations estimated from tilted-ring fits to the interferometric data cubes, the errors on which are calculated as the maximum difference from the best value obtained when using only one-half of the galaxy velocity field. Column (8) lists our adopted best inclinations, as described in Section 2.6.1. Column (9) contains the K_s -band magnitudes from the 2MASS (Skrutskie et al. 2006), converted to absolute magnitudes using the distance to each galaxy adopted for the ATLAS^{3D} survey in Paper I. These distances are drawn preferentially from Mei et al. (2007) and Tonry et al. (2001). We assign to the absolute magnitudes an error of ± 0.1 mag, taking into account distance uncertainties, which completely overwhelm errors caused by the lack of an internal extinction correction. Columns (10) and (11) list the galaxies with boxy CO profiles, as determined from the visual inspection of the single-dish spectra (Column 9), and a combination of single-dish and interferometric data where available (Column 11). A question mark indicates that with the respective data we are unable to determine if the profile is boxy, and hence do not include it. The telescope used to obtain the interferometric data is indicated in Column (12), where C = CARMA, P = PdBI, B = BIMA and O = OVRO. Column (13) lists the relevant references for the interferometric observations, and in two cases (NGC 2685 and 4753) references for the inclination measurements: (1) Alatalo et al. (in preparation); (2) Crocker et al. (2011); (3) Young et al. (2008); (4) Józsa et al. (2009); and (5) Steiman-Cameron et al. (1992).

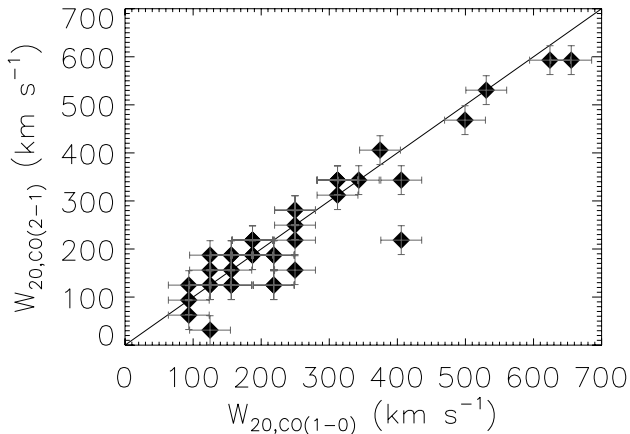


Figure 1. A comparison between CO(1–0) and CO(2–1) single-dish linewidths measured as described in Section 2.3. The solid line shows the one-to-one relation. Linewidths are discretized due to the 30 km s^{-1} channel width.

estimated to be robust to within half a channel width, $\approx 15 \text{ km s}^{-1}$, and are listed in Table 1.

2.4 Interferometric data

As part of the ATLAS^{3D} survey, all CO(1–0) detections with an integrated flux greater than about 19 Jy km s^{-1} that do not have interferometric maps available in the literature are to be observed with the Combined Array for Research in Millimeter-wave Astronomy (CARMA; Bock et al. 2006). Full details of this ongoing interferometric survey can be found in Alatalo et al. (in preparation), but we summarize the observations here.

Observations of the sample galaxies have been ongoing since early 2008, mainly in the D-array configuration, providing a spatial resolution of 4–5 arcsec. CO(1–0) has so far been observed using narrow-band correlator configurations, providing at least three raw channels per 10 km s^{-1} binned channel whilst ensuring adequate velocity coverage for all galaxies. Bright quasars were used to calibrate the antenna-based gains and for passband calibration. The data were calibrated and imaged using the MIRIAD (Multichannel Image Reconstruction, Image Analysis and Display) software package (Sault, Teuben & Wright 1995). Total fluxes were compared with the IRAM 30-m single-dish observations to ensure that large proportions of the fluxes were not being resolved out.

A total of 22 galaxies included in this work have been observed with the CARMA so far (IC 0676, IC 719, IC 1024, NGC 1222, 1266, 2764, 2824, 3626, 3665, 4119, 4292, 4324, 4429, 4435, 4694, 4710, 5379, 6014 and 7465, PGC 058114, UGC 06176 and UGC 09519). We also include here the galaxies for which data are already available from the literature, mostly from SAURON survey (de Zeeuw et al. 2002) follow-ups. These are NGC 3032, 4150, 4459 and 4526 (Young et al. 2008), NGC 2685 (Schinnerer & Scoville 2002), NGC 2768 (Crocker et al. 2008), NGC 0524, 3489 and 4477 (Crocker et al. 2011). This makes for a total of 31 sample galaxies that have interferometric data.

The data cubes were summed spatially to measure total fluxes and revised values for W_{20} , serving as consistency checks on the values derived from the single-dish data. The large primary beam of the arrays also allows us to take better measurements for the small subset of galaxies in which a substantial part of the CO distribution was missed by the 23 arcsec beam of the IRAM 30-m telescope, such

as in IC676, NGC 4324, 4477, 4710 and 7465, and PGC 058114. This can be due to pointing errors or molecular gas distributions that extend beyond the beam. The integration time for the single-dish CO observations was adjusted to obtain a fixed noise level and as such galaxies that are only detected at $\approx 5\sigma$ will have rather uncertain W_{20} linewidths. The interferometric observations in these cases (NGC 2685, 2768, 3489 and 4477) will provide a better constraint on the linewidths. The revised W_{20} values are listed in Table 1, but for consistency these velocities are only used in the TFRs presented in Sections 4.1.3 and 4.1.4.

2.5 Inclination correction

The measured quantity W_{20} is a projection of the gas velocity into the line of sight. If this is to be used for a TF analysis, then it must be deprojected. Many methods for the inclination measurement are available. Starting with the simplest, we compare various methods below in order of increasing complexity, to allow future CO-TFR surveys to select the optimum method for their needs. The methods presented in Sections 2.5.1 and 2.5.2 use only single-dish molecular data, whilst the method presented in Section 2.5.3 requires interferometric maps.

2.5.1 Galaxy axial ratio

A rough measurement of the inclination can be obtained by estimating the axial ratio of the stellar distribution of the host galaxy from imaging data:

$$i_{b/a} = \cos^{-1} \left(\sqrt{\frac{q^2 - q_0^2}{1 - q_0^2}} \right), \quad (1)$$

where q is the ratio of the semiminor (b) to the semimajor (a) axis of the galaxy and q_0 is the intrinsic axial ratio when the galaxy is seen edge-on ($q_0 \equiv c/a$). q_0 is often assumed to be 0.2 in disc galaxies (Tully & Fisher 1977), but early types can have large bulge-to-disc ratios leading to a large uncertainty in any assumed value of q_0 .

Various lines of enquiry suggest a mean q_0 value of ≈ 0.34 for the fast rotators in the ATLAS^{3D} sample (Weijmans et al., in preparation), which we adopt here. The intrinsic scatter around this value will introduce an artificial increase in the TFR scatter, but the effect is very small. Indeed, we stress that this q_0 -related inclination correction is only significant in highly inclined galaxies, where, fortunately, inclination errors have the smallest effect on the deprojected velocities and thus the derived TFR. For example, assuming $q_0 = 0$ for the current sample would only change the zero-point of the derived TFR by 0.02 dex along the velocity axis and it does not change the gradient.

The CO-detected ETGs in this work are all fast rotators. Even the fast-rotating (morphologically classified) E galaxies have well-defined kinematic axes, meaning that defining an inclination angle has a physical meaning (see Emsellem et al. 2011, hereinafter Paper III). It is also important to note that using this method to correct the CO velocity widths for a TF analysis implicitly assumes that the CO is distributed in the same plane as the galaxy major-axis. A recent work by Davis et al. (in preparation), however, suggests that a sizeable proportion of ETGs have molecular gas misaligned with respect to the stellar kinematic axis, so in these cases one expects this method to introduce additional artificial scatter in the TFR.

The value of $i_{b/a}$ obtained by assuming $q_0 = 0.34$ for each galaxy is listed in Table 1. These values were calculated using equation (1) with the mean galaxy axial ratio reported in the NASA/IPAC Extragalactic Data base (NED). These values are the mean of the measurements from the Sloan Digital Sky Survey (SDSS) in the r band, 2MASS at the K_s band (Skrutskie et al. 2006), and blue and red filters from both the Third Reference Catalogue of Bright Galaxies (RC3; de Vaucouleurs et al. 1991) and the Uppsala General Catalogue of Galaxies (UGC/POSS; Nilson 1973) where available. The exceptions to this are NGC 3665, where the axial ratio is based only on superior SDSS imaging, and PGC 058114, where the mean value of the axial ratio from the HyperLeda data base (Paturel et al. 2003) has been used, due to a larger number of available measurements. When these inclinations are compared to those estimated from the axial ratios of Krajnović et al. (2011) (hereinafter Paper II; derived by calculating the moments of inertia of the surface brightness distribution from the SDSS and Isaac Newton Telescope (INT) r -band images) for the galaxies in the ATLAS^{3D} sample, they are found to agree well.

2.5.2 Dust axial ratio

It should be possible to obtain more accurate inclination estimates from fitting ellipses to the dust highlighted in unsharp-masked optical images of the galaxies. This method has several advantages over galaxy axial ratios. Dust distributions typically have very small vertical scaleheights; hence, equation (1) with $q_0 = 0$ should yield a good estimate of their inclinations. It has also been shown that CO and dust in ETGs are usually spatially coincident (Crocker et al. 2008, 2009, 2011; Young et al. 2008); hence, the inclination of the dust (i_{dust}) should trace the true inclination of the molecular gas. This is especially useful where the molecular gas and stars are misaligned.

Unsharp-masked dust maps were created for all the galaxies in this work, preferentially from archival *Hubble Space Telescope* (*HST*) images or where these were not available from SDSS g -band (Adelman-McCarthy et al. 2008) or ATLAS^{3D} INT Wide Field Camera r -band images (Scott et al., in preparation). Ellipses were then fitted by eye to the resulting maps and the inclination of the dust calculated from equation (1) with $q_0 = 0$. Four example galaxies are shown in Fig. 2.

One of the galaxies (NGC 4753) is well studied in the literature, showing many thin filamentary dust features that are well fitted by a model featuring an inclined disc, twisted by the differential precession, with an average $i_{\text{dust}} = 75^\circ \pm 3^\circ$ (Steiman-Cameron, Kormendy & Durisen 1992). We adopt this value here. A full list of i_{dust} values can be found in Table 1.

2.5.3 Molecular gas modelling

Tilted-ring analyses have been used to determine the geometric and kinematic parameters of neutral and molecular gas discs in interferometric data for many years (e.g. Rogstad, Lockhart & Wright 1974; Christodoulou, Tohline & Steiman-Cameron 1988; Koribalski et al. 1993). In this work, we have made use of the Groningen Image Processing System (GIPSY) add-on package TiRiFiC, described in Józsa et al. (2007) to fit tilted-ring models to observed data cubes. Due to the small number of independent synthesized beams across our typical sources, an unwarped disc model was fitted where the inclination, position angle, systemic velocity and kinematic centre of the gas were varied globally, and only the velocity and surface

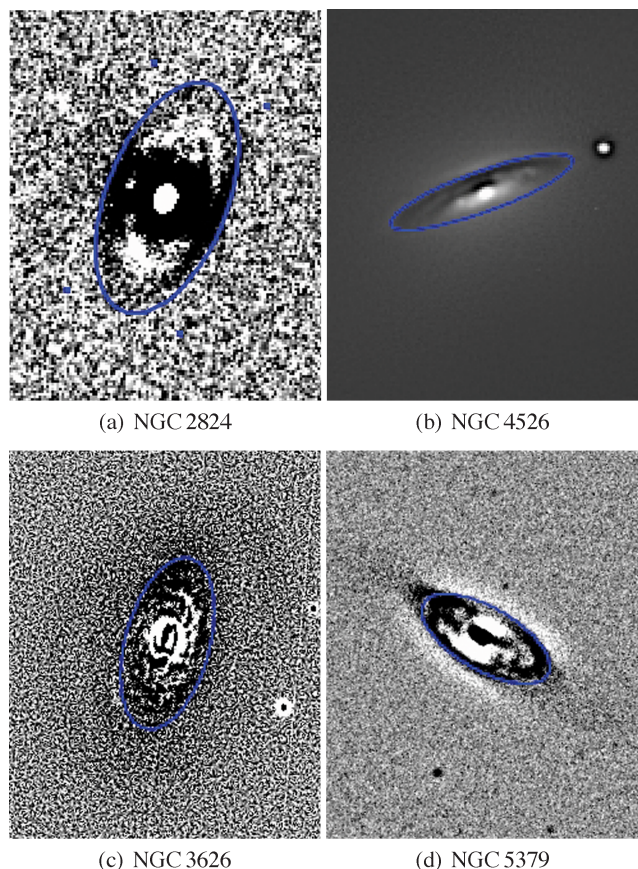


Figure 2. Four examples of unsharp-masked images picking up dusty spiral structures and rings. Overlaid in blue are the best-fitting ellipses from which we estimate the dust inclination.

brightness were allowed to vary radially (i.e. for each ring). Full details of the fits are reported in Davis et al. (in preparation), but the inclination measures (i_{mol}) used in this work are listed in Table 1. The error quoted for each galaxy is the maximum inclination difference found if each side of the velocity distribution is supplied as an input to the fitting program separately.

We have attempted the analysis described above for all the mapped galaxies in our sample in which we have adequate spatial resolution, with one exception where we felt the literature value was sufficient. NGC 2685 has dust lanes which look polar on the north-east side and are coincident with the H γ , H α and CO emission (Schinnerer & Scoville 2002). This system has been revealed to feature a coherent, extremely warped disc (Józsa et al. 2009), for which we adopt the published average inclination value of $i_{\text{mol}} = 69^\circ \pm 9^\circ$.

2.6 W_{20} linewidths

The velocity widths calculated as described in Sections 2.3 and 2.4 are an approximation to (twice) the maximum rotational velocity of CO. To be useful, these CO measurements must reach beyond the peak of the galaxy rotation curves. Young et al. (2008) suggest that the molecular gas in early types is often centrally concentrated and hence this requirement is not trivially fulfilled.

One sign of a tracer having reached a flat part of a galaxy rotation curve is a classic ‘double-horned’ velocity profile. Lavezzi & Dickey (1997) discuss in detail the problem of recovering velocity

widths from CO observations, given the variety of profile shapes typically seen in millimetre observations. They show that CO profile shapes are affected by the extent of the emitting gas, the beam size of the telescope, pointing errors and the optical depth of the molecular material. CO linewidths are shown to accurately retrieve V_{flat} in the majority of cases where the flaring parameter $R_{2,5}$ (the ratio of the velocity widths measured at 20 and 50 per cent of the peak) is less than 1.2 (Lavezzi & Dickey 1997, 1998). This criterion effectively selects galaxies that show a boxcar, or double-horned, profile shape with sharp edges and rejects those with a more Gaussian profile. We follow this methodology in this work, exclusively using galaxies with double-horned/boxcar/sharp-edged profiles, which, hereinafter, we will refer to as ‘boxy’, assuming that in these systems the measured gas velocity width will approximate the velocity beyond the peak of the circular velocity curve.

The limited signal-to-noise ratio of the spectra we possess, however, means that the value of the flaring parameter discussed above is often rather uncertain. We performed several other tests, attempting to find a good automatic way of classifying boxy velocity profiles. These included fitting single Gaussians and selecting those galaxies that showed significant structure in the residuals, and fitting Gauss–Hermite polynomials and looking for a significant kurtosis ($h_4 < 0$). Both of these methods worked well for wide lines and high-signal-to-noise-ratio cases, but in the case of narrow lines, or low-signal-to-noise-ratio cases, the fits were not well constrained. In these cases, the different methods often produced contradictory results and/or did not agree with a careful classification by eye. In future surveys with better data quality, or large numbers of objects (so one can afford to remove low-signal-to-noise-ratio detections), these methods will likely to be very useful, but in this work, with a limited number of objects, we prefer a careful classification by eye.

Even by eye, some cases are hard to classify, especially when the profiles are narrow as the galaxies are fairly face-on or if the signal-to-noise ratio is low. We cautiously use only those galaxies with clear boxy profiles here, flagging the 12 galaxies with uncertain profiles shapes.

Using this profile shape criterion is likely to introduce some uncertainties, for example, galaxies with a molecular ring will have double-horned profiles without the CO necessarily having reached beyond the peak of the rotation curve. Similarly, galaxies that have strong resonances may have their gas distribution truncated at the turnover radius, causing them to not display a classic boxy shape even though the edge of the distribution is rotating at the turnover velocity. In Section 3.1, we use the dynamical models available to us from the ATLAS^{3D} survey to quantify these biases.

2.6.1 Combining interferometric and single-dish data

Finally, we can combine our single-dish and interferometric observations using all available data to increase the number of galaxies with high-quality measurements available. When available, we thus always use interferometric velocity widths and, when well constrained, interferometric inclinations (quantitatively, we select galaxies with inclination errors less than 6°). For the remaining galaxies, we preferentially use dust inclinations or, failing this, b/a inclinations. We can also use the interferometric data when available to help ascertain which galaxies have reached beyond the peak of the rotation curve, in conjunction with the usual single-dish boxy criterion. This hybrid measure represents our best estimate of the

inclination and velocity width. The adopted best inclinations are listed in Table 1.

3 COMPARISON WITH OTHER VELOCITY MEASURES

3.1 Model circular velocity curves

As alluded to in Section 2.6, it has yet to be established for a large sample of ETGs that single-dish CO is a good tracer of the circular velocity. One would like to test this and attempt to quantify the biases introduced by using the profile shape as a proxy for reaching beyond the peak of the circular velocity curve. As Williams et al. (2010) discuss, one must be careful when comparing velocity measures derived from different methods, as they are likely to have significant systematic differences. However, it is important to ascertain that the CO linewidths vary systematically, in a similar way to other rotation measures.

The gravitational potential of ETGs can also be significantly different from that of spirals. ETGs often have circular velocity profiles with high peaks at small radii that decline before flattening out. The W_{20} linewidth is, in general, more sensitive to the peak velocity of the molecular gas, rather than the flat part of the rotation curve, unless the gas disc is sufficiently extended. This would lead to an overestimation of the velocity width. This problem has been discussed in detail by Noordermeer & Verheijen (2007), who find that using the H I peak velocity in massive early-type spirals results in an offset TFR. They report that the asymptotic velocity is a better measure of the total potential and results in spirals of all masses lying on a single TFR.

An estimate of the amount by which we may be overestimating the velocity widths can be obtained using the circular velocity curves produced by Williams, Bureau & Cappellari (2009) from the stellar dynamical modelling of their S0 galaxies. The median value of the circular velocity curve after the peak out to the maximum extent of the data, where the model is well constrained, is adopted as a measure of the velocity of its flat part [in the case of Williams et al. (2009) their data extend to $\approx 3R_c$]. When tested on the S0 circular velocity curves from Williams et al. (2009), this median performs well in picking out the velocity of the flat section. The mean ratio of the peak velocity to the flat velocity is 1.15 or 0.06 dex. When transformed to an offset in the luminosity using the parameters of the best-fitting S0 TFR of Williams et al. (2010), this effect corresponds to an offset of upto 0.5 mag at the K_s band. This is approximately half of the ≈ 1 mag offset observed by various authors between the spirals and ETGs, and is thus significant if not properly accounted for.

In order to test the assumption that our ETGs with boxy profiles have gas distributions that reach beyond the peak of the circular velocity curve and to see if our linewidths are overly sensitive to the peak velocity, like Williams et al. (2009, 2010) we utilize the axisymmetric Jeans anisotropic dynamical modelling (JAM) method described in Cappellari (2008). Some examples of the approach, using SAURON integral-field kinematics (Emsellem et al. 2004) as done here, are presented in Scott et al. (2009). For the ATLAS^{3D} survey a multi-Gaussian expansion (MGE; Emsellem, Monnet & Bacon 1994) was fitted to the SDSS (Abazajian et al. 2009) or INT photometry (Scott et al., in preparation). The MGEs were then used to construct JAM models for all the 260 ATLAS^{3D} galaxies (see Cappellari et al. 2010) which were fitted to the SAURON stellar kinematics (Paper I). The models have three free parameters: the

inclination (i_{JAM}), the M/L assumed to be spatially constant and the anisotropy $\beta_z = 1 - \sigma_z^2/\sigma_R^2$, which is also assumed to be spatially constant. From each mass model, we have calculated the predicted circular velocity curve in the plane of the galaxy. It is worth bearing in mind that, where CO is misaligned from the plane of the galaxy, we are thus making implicit assumptions about the symmetry of the matter distribution. As these models include no dark matter, the circular velocity often declines at large radii and one must be careful to measure the circular velocity at a suitable radius (i.e. where we have constraining data) when comparing to the observations.

Analysis of the ATLAS^{3D} interferometric observations, presented in Davis et al. (in preparation), suggests that the average radial extent of CO discs in ETGs is around one optical effective radius (the radius encompassing half of the light); hence, the circular velocity measured at one effective radius (denoted by $V_{\text{JAM,Re}}$) is a sensible quantity to be used for comparison. The effective radius used here is a combination of the values from the 2MASS (Skrutskie et al. 2006) and RC3 (de Vaucouleurs et al. 1991), as described in Paper I. For galaxies where interferometric observations are available, we have also calculated the model circular velocity at the maximum extent of CO and denote this by $V_{\text{JAM,Rco}}$. Both values can be found in Table 2.

We compare the two model circular velocity measures described above with the measured CO linewidths in Fig. 3. The linewidths of the galaxies with boxy CO profiles correlate well with the circular velocities measured at both one effective radius (R_e) and the radius of the maximum CO extent (R_{CO}). The offset from $V_{\text{JAM,Re}}$ is 0.01 ± 0.02 dex, the data points displaying an rms scatter of 0.1 dex. The galaxies that do not have boxy CO profiles have linewidths systematically smaller than those predicted from the models in most cases, suggesting that their CO has been correctly identified as not reaching beyond the peak of the rotation curve. The comparison with $V_{\text{JAM,Rco}}$, albeit with smaller number statistics, shows that the difference between the model and the CO linewidths is again consistent with the models, with a mean offset of 0.002 ± 0.02 dex and a rms scatter of 0.1 dex. There is no systematic behaviour in the residuals for the boxy galaxies in either plot. The galaxies that do not have boxy CO profiles are closer to the JAM model predictions, but do not lie on the one-to-one relation as expected, with a mean offset of -0.07 ± 0.05 dex. This offset is likely because the CO in these objects is very compact and beam effects mean the CO size is overestimated. The JAM model velocities have thus been estimated at the wrong radius. The one galaxy which does not have a boxy profile, but has a linewidth larger than the predicted circular velocity, is NGC 1266, recently discovered to have a kiloparsec-scale molecular outflow (Alatalo et al., in preparation).

To check if our linewidths are overly sensitive to the peak of the rotation curve, we also extract from the JAM models the maximum of the circular velocity curve, denoted by $V_{\text{JAM,max}}$, and the median value of the circular velocity curve, measured between the peak and the maximum extent of the SAURON data ($\approx 1R_e$), denoted by $V_{\text{JAM,>peak}}$. As discussed above, defining $V_{\text{JAM,>peak}}$ in this way picks out the value of the flat part of the rotation curve well in tests based on the data of Williams et al. (2009), which extend to $\approx 3R_e$. Our data are only constrained out to around $\approx 1R_e$, but the rotation curves do not drop wildly in this region. It should, however, be noted that this measure may not be the same as the velocity measured at very large radii. The values of $V_{\text{JAM,max}}$ and $V_{\text{JAM,>peak}}$ can be found in Table 2.

Table 2. Parameters extracted from the JAM model circular velocity curves for the ATLAS^{3D} early-type CO-rich galaxies used in this paper.

Galaxy	$V_{\text{JAM,Re}}$ (km s ⁻¹)	$V_{\text{JAM,Rco}}$ (km s ⁻¹)	$V_{\text{JAM,max}}$ (km s ⁻¹)	$V_{\text{JAM,>peak}}$ (km s ⁻¹)
(1)	(2)	(3)	(4)	(5)
IC 0676	117	116	118	116
IC 0719	232	232	233	218
IC 1024	150	163	174	157
IC 2099	–	–	–	–
NGC 0524	337	362	368	337
NGC 1222	177	177	236	177
NGC 1266	141	116	144	134
NGC 2685	160	–	186	160
NGC 2764	199	190	207	196
NGC 2768	320	325	342	311
NGC 2824	220	220	278	206
NGC 3032	129	158	238	135
NGC 3182	183	–	198	178
NGC 3489	169	197	198	159
NGC 3619	216	–	277	223
NGC 3626	173	187	256	174
NGC 3665	358	354	362	321
NGC 4150	134	141	163	131
NGC 4270	185	–	193	182
NGC 4292	–	–	–	–
NGC 4309	–	–	–	–
NGC 4324	150	152	169	150
NGC 4429	276	276	294	273
NGC 4435	237	263	266	237
NGC 4459	244	261	273	244
NGC 4477	249	278	295	249
NGC 4526	328	338	348	292
NGC 4684	136	–	137	123
NGC 4694	96	–	99	93
NGC 4710	175	161	202	176
NGC 4753	301	–	302	274
NGC 5173	180	–	202	166
NGC 5273	127	–	148	125
NGC 5379	152	–	158	147
NGC 6014	148	149	185	148
PGC 29321	154	–	165	154
PGC 56772	152	–	153	133
PGC 58114	–	–	–	–
PGC 61468	166	–	166	160
UGC 05408	139	–	163	133
UGC 06176	184	196	219	184
UGC 09519	160	165	182	155

Notes. This table contains the circular velocities derived from the JAM models, extracted at different radii. Galaxies that were removed from the ATLAS^{3D} sample have no JAM model available. Column (2) contains the circular velocities extracted at one effective radius. Column (3) contains the circular velocities extracted at the maximum radial extent of the CO, or 12 arcsec, whichever is smaller. Galaxies without interferometric observations are not included. Column (4) contains the maximum circular velocity. Column (5) contains the median of velocities after the peak in the circular velocity curve out to the maximum radius at which the model is constrained by the observational data. Some galaxies had insufficient data to constrain such a median between these two points and are excluded. The error on these JAM velocities is estimated to be ≈ 8 per cent. This is a combination of an average 5 per cent error in the observed stellar velocity dispersion constraining the models and model errors of ≈ 6 per cent (Cappellari et al. 2006). This does not include errors in the inclination, which are harder to quantify.

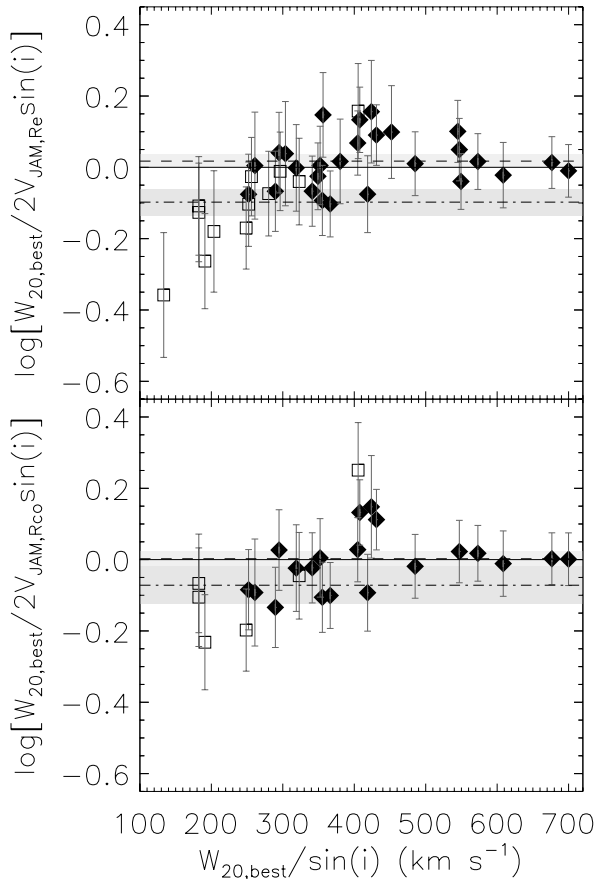


Figure 3. Difference between our best CO linewidths deprojected using the best inclinations (as described in Section 2.6.1) and twice the JAM model circular velocities, measured at one effective radius (top panel) and the radius of the maximum CO extent or 12 arcsec, whichever is smaller (bottom panel), plotted against the best inclination deprojected CO velocity width. Galaxies with boxy profiles are plotted as the filled diamonds, while the others are shown as the open squares. The solid line indicates where the JAM and CO velocities are identical. The dashed line and dot-dashed line are fitted offsets from zero for the boxy galaxies and the other galaxies, respectively. The errors on the fits are indicated as the shaded regions around the best-fitting lines.

The top panel of Fig. 4 shows a comparison between the observed CO linewidths, deprojected using dust inclinations (as described in Section 2.5.2), and $V_{\text{JAM,max}}$. The CO linewidths are systematically smaller than the maximum of the circular velocity curve. The median peak of the JAM circular velocity curves is at 8.5 arcsec, well within the single-dish beam, and hence we do not expect the systematically missed emission to cause this trend. The mean offset from the maximum value is -0.03 ± 0.02 dex, broadly similar to the offset between the maximum and the flat part of the circular velocity curve expected from the results of Williams et al. (2009). The rms scatter around this value is 0.09 dex. This suggests that we are not overly sensitive to the peak of the circular velocity curve. The galaxies which do not have boxy profiles are again offset to much lower velocities. The only galaxy whose linewidth is inconsistent with the maximum value of its predicted circular velocity curve is again NGC 1266.

The bottom panel of Fig. 4 compares the observed CO linewidths, deprojected using dust inclinations, with $V_{\text{JAM,>peak}}$. The CO measurements for galaxies with double-horned profiles are, within the

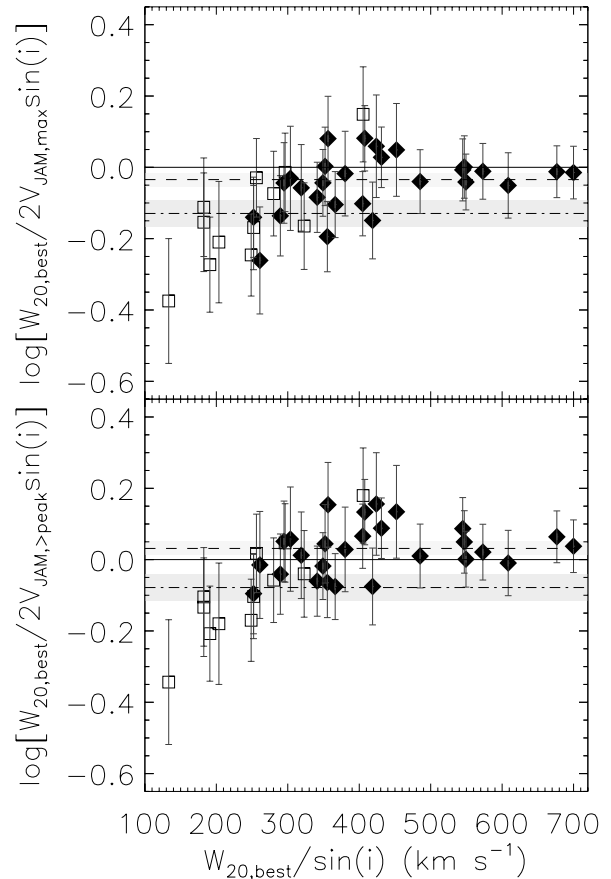


Figure 4. Same as Fig. 3, but for JAM model circular velocities measured at the maximum (top panel) and using the median velocity after the maximum (bottom panel).

errors, consistent with the $V_{\text{JAM,>peak}}$ measure. The mean offset from this measure is 0.02 ± 0.02 dex, with a rms deviation of 0.1 dex. The galaxies that were not identified as boxy are on average offset from $V_{\text{JAM,>peak}}$ by -0.1 ± 0.04 dex. There are several galaxies that do not have a boxy profile, but are consistent with rotating at $V_{\text{JAM,>peak}}$. These galaxies are NGC 4684, PGC 56772 and PGC 61468, all of which have profiles which were hard to classify. If interferometric observations were available, we would then expect to find that the gas does indeed reach beyond the peak of the galaxy rotation curve in these systems.

Figs 3 and 4 demonstrate that, if one selects galaxies with boxy profiles, W_{20} velocity widths provide a good estimate of the circular velocity after the inner peak of the rotation curve, whether estimated as $V_{\text{JAM,Re}}$ or $V_{\text{JAM,>peak}}$. It is worth mentioning that, for our sample, a simple cut excluding galaxies with CO linewidths $\lesssim 250 \text{ km s}^{-1}$ would have a similar effect to selecting by the profile shape, removing most of the outliers. Applying an arbitrary cut in velocity, the most important TF parameter, could bias the derived TFR, especially for a sample selected in a different way, and hence we prefer the selection by the profile shape in this work.

3.2 H I linewidths

Morganti et al. (2006) and Williams et al. (2010) have shown that in some cases H I linewidths are not a good measure of the circular velocity for ETGs. We examine this here by retrieving archival H I

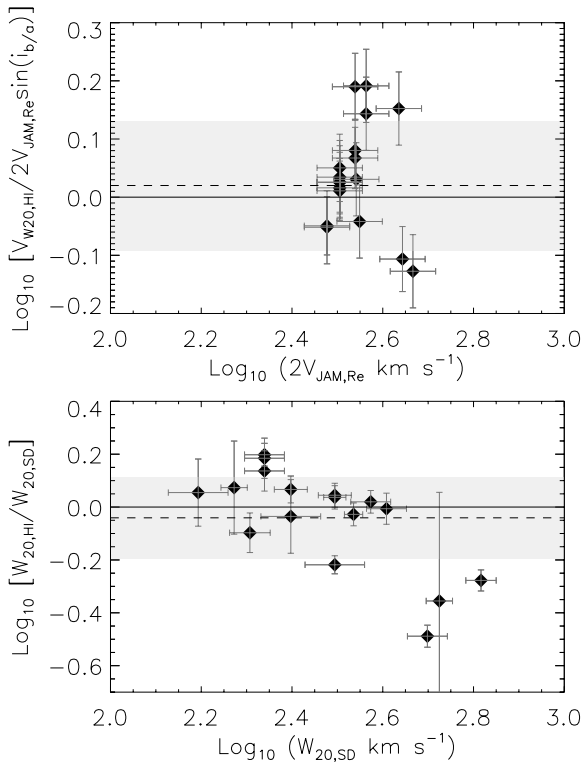


Figure 5. Top panel: difference between the deprojected H I linewidth and twice the JAM model circular velocity measured at one effective radius, for galaxies with archival H I data in the HyperLEDA data base, as a function of the model velocities. The solid line indicates where the JAM and H I velocities are identical. The dashed line is the mean difference, with the rms scatter indicated in grey. Bottom panel: as for the top panel, but comparing observed CO single-dish and H I linewidths, for galaxies with boxy CO profiles only.

single-dish linewidths measured at 20 per cent of the peak flux from HyperLEDA (Paturel et al. 2003, denoted by $W_{20,H I}$).

In Fig. 5, we compare the single-dish H I linewidths to twice the projected JAM circular velocities measured at R_e (top panel) and the observed CO linewidths (bottom panel). All galaxies from our sample with archival H I data at the time of the retrieval are included. We find that although the average difference between the H I linewidth and the JAM circular velocities is small (0.02 dex), the scatter is large (rms scatter of ≈ 0.11 dex) and the single-dish H I linewidths do not correlate statistically with the galaxy luminosity. The same is true when one compares with observed CO linewidths, with a larger scatter (≈ 0.15 dex). There is also a systematic trend in the residuals in the bottom panel of Fig. 5, where the galaxies with high CO rotation velocities, which are likely of high masses, have systematically smaller H I linewidths.

Fig. 5 suggests that some of the detected H I sources, at high CO velocities (and hence likely at high mass), are either not related to the galaxy under study or that H I has been kinematically disturbed. This is consistent with the results of Morganti et al. (2006), Williams et al. (2010) and Serra et al. (in preparation).

Single-dish H I linewidths in the HyperLEDA data base are, however, known to suffer from many issues, including major problems with the source confusion. Outer H I discs are also usually warped with respect to the inner regions and hence a simple inclination estimate from optical images will be insufficient. Interferometric H I data allow one to identify relaxed discs and in these the rotation and

TFR can be studied (e.g. Morganti et al. 2006; Oosterloo et al. 2007; Weijmans et al. 2008; Oosterloo et al. 2010). To further investigate the TFR, and the disc–halo conspiracy in these galaxies, a future paper in this series will study the H I TFR of ETGs at large radii using superior interferometric H I data.

4 RESULTS

Using the data presented in Table 1, we construct a series of TFRs to explore the effect of the different inclination and velocity measurements, defined in the order of increasing complexity. The results are shown in Fig. 6. The general form of the K_s -band TFR we have adopted is

$$M_{K_s} = a \left[\log_{10} \left(\frac{W_{20}}{\text{km s}^{-1}} \right) - 2.6 \right] + b, \quad (2)$$

where a is the slope and b is the zero-point of the relation.

The package MPFIT (Markwardt 2009) was used to fit the inverse of equation (2) (regressing the observed rotation velocities) with the addition of an intrinsic scatter, which we iteratively adjust to ensure a reduced $\chi^2 \approx 1$. Full details of the fitting procedure can be found in Williams et al. (2010).

Each plot in Fig. 6 shows two best-fitting lines. For the first we allow both the intercept and the slope to vary, while for the second, we fix the slope to that found by Tully & Pierce (2000), $a = -8.78$. For reference, we also plot the K -band spiral galaxy TFR of Tully & Pierce (2000) (see equation 3), which was constructed using H I linewidths of spiral galaxies in 12 well-separated clusters, and the K_s -band S0 TFR from Williams et al. (2010) (see equation 4), which was derived from the Jeans modelling of major-axis stellar kinematics from 14 edge-on S0 galaxies:

$$M_{K_s} = -8.78 \left[\log_{10} \left(\frac{W_{20}}{\text{km s}^{-1}} \right) - 2.5 \right] - 23.17, \quad (3)$$

$$M_{K_s} = -8.56 \left[\log_{10} \left(\frac{W_{20}}{\text{km s}^{-1}} \right) - 2.4 \right] - 24.02. \quad (4)$$

4.1 CO Tully–Fisher relations

4.1.1 Inclinations from galaxy axial ratios

The CO-TFR deprojected using $i_{b/a}$ is presented in the top two panels of Fig. 6. The parameters of the best-fitting relations are listed in Table 3. The top left-hand panel shows all galaxies, with the open squares for those which do not show a boxy CO profile or where the profile shape is unclear and the solid triangles for those with clear boxy profiles. Only a loose correlation is observed, with clear outliers, almost all of which are galaxies without double-horned profiles. A much tighter correlation is observed, once galaxies with non-boxy profiles are removed, as shown in the top right-hand panel. This is physically motivated, as we believe that the gas in these galaxies does not reach beyond the peak of the rotation curve. Once the non-doubled-horned galaxies are removed, both best-fitting lines agree within the errors with the TFR of Williams et al. (2010), providing strong a posteriori evidence that CO in these galaxies does trace the circular velocity in a way that is consistent with dynamical models. The remaining outlier is NGC 7465 which we will discuss in more detail below. If this outlier is removed, then the best-fitting relation follows that of Williams et al. (2010) even more closely. The intrinsic scatter of the best-fitting relation with a

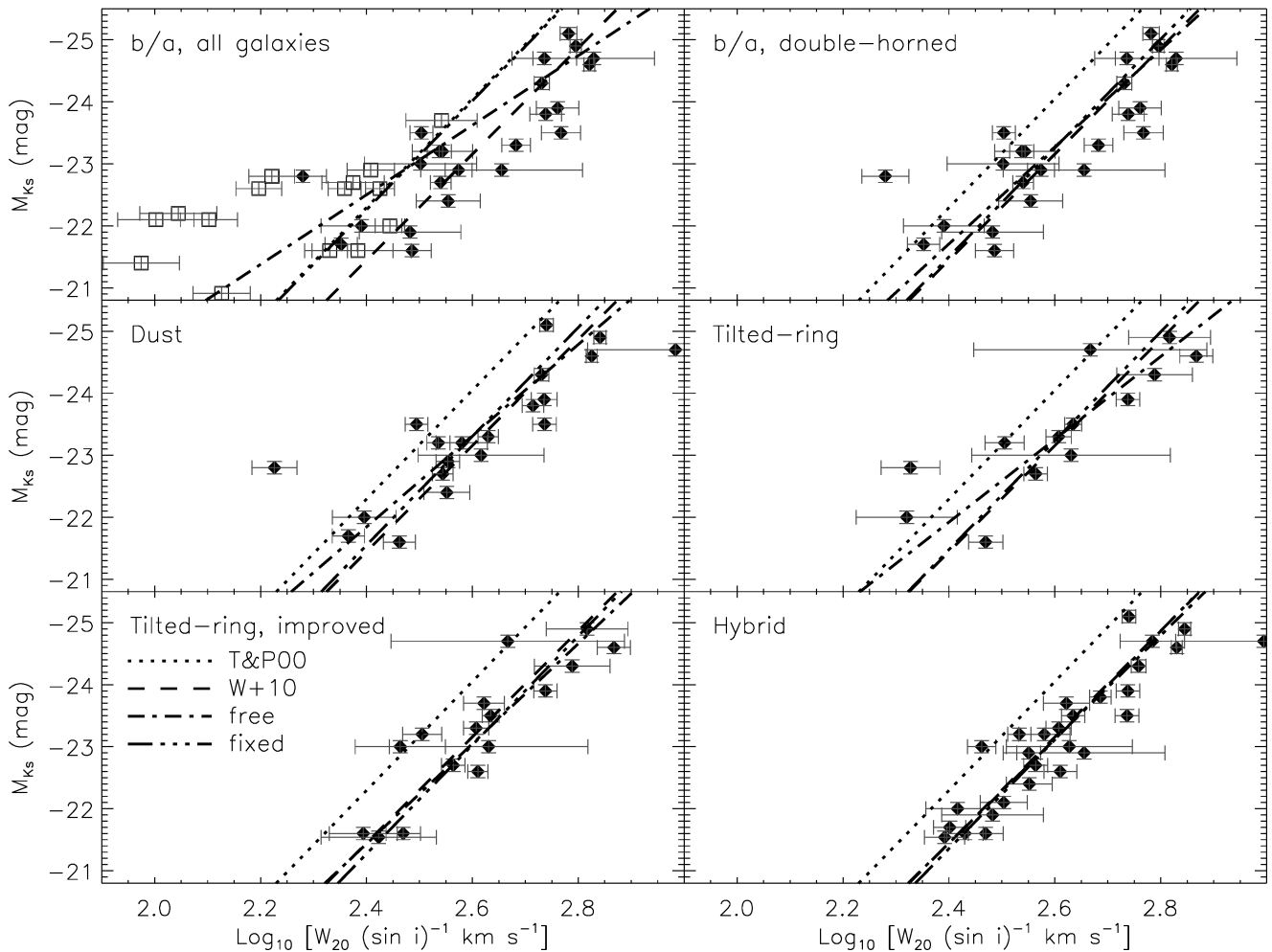


Figure 6. CO-TFRs constructed using various inclination and linewidth measurements. The correlations shown in each plot and indicated in the legend are the spiral galaxy TFR of Tully & Pierce (2000), derived from H I linewidths (short dashes), and the S0 TFR of Williams et al. (2010), derived from Jeans modelling (long dashes). Also plotted are the best-fitting relations for our data, of the form given in equation (2), for both an unconstrained fit (dot-dashed line) and a fit where the slope is fixed to that found by Tully & Pierce (2000) (triple dot-dashed line). The best-fitting parameters are listed in Table 3. Top left-hand panel: inclinations derived from galaxy optical axial ratios (see Section 2.5.1). CO detections with boxy profiles are shown as the filled diamonds and galaxies with non-boxy profiles and uncertain classifications are shown as the open squares. Top right-hand panel: the same as the top left-hand panel, but galaxies with non-boxy profiles are removed. The outlier is NGC 7465. Middle left-hand panel: the same as the top right-hand panel, but using inclinations from unsharp-masked dust images (see Section 2.5.2). The outlier is again NGC 7465. Middle right-hand panel: the same as the top right-hand panel, but using interferometric W_{20} values and inclinations derived from tilted-ring fits to the interferometric data (see Section 2.5.3). Bottom left-hand panel: the same as the middle right-hand panel, but using the interferometric data to identify galaxies with CO which reaches beyond the peak of the galaxy rotation curve. Bottom right-hand panel: a hybrid plot using the best inclinations and velocity widths as defined in Section 2.6.1. Both best-fitting lines overlay the relation of Williams et al.

free and a constrained slope is 0.57 and 0.63 mag with the total rms scatters of 0.69 and 0.78 mag, respectively.

4.1.2 Inclinations from dust axial ratios

In a similar way, we can construct a TFR using the inclinations derived from fitting ellipses to the dust distributions highlighted in unsharp-masked images. The CO-TFR deprojected using i_{dust} is presented in the middle left-hand panel of Fig. 6. Once again, within the quoted errors, the best-fitting relations are consistent with the result of Williams et al. (2010). The parameters of the best-fitting relations are listed in Table 3. The intrinsic scatter of the best-fitting relation with a free and a constrained slope is 0.65 and 0.78 mag, but with the total scatter of 0.75 and 0.94 mag, respectively. The outlier

is NGC 7465 – without this galaxy the observed intrinsic scatter in the unconstrained fit decreases to 0.46 mag, with the total scatter of 0.6 mag, confirming the visual impression that the correlation using dust inclinations is tighter. Removing this galaxy also improves the agreement between our best-fitting slope and that found by Williams et al. (2010).

4.1.3 Inclination from molecular gas modelling

Using the inclinations from the tilted-ring models and the total velocity widths calculated from the interferometric data, we can construct yet another TFR. First, we do this naively, using only the single-dish boxy classifications. This results in the middle right-hand panel of Fig. 6. Some of the interferometric observations have

Table 3. Best-fitting parameters of the TFRs shown in Fig. 6.

Inclination method (1)	a (mag) (2)	b (mag) (3)	σ_{intr} (mag) (4)	σ_{total} (mag) (5)	$W_{20,\text{sd}}$ (6)	$W_{20,\text{inter}}$ (7)	Selection (8)
Stellar bla	-5.61 ± 0.71	-23.62 ± 0.16	0.75	0.82	x	–	None
Stellar bla	–	-24.01 ± 0.23	1.30	1.42	x	–	None
Stellar bla	-7.82 ± 1.12	-23.27 ± 0.15	0.60	0.69	x	–	SD
Stellar bla	–	-23.25 ± 0.16	0.66	0.78	x	–	SD
Dust	-7.36 ± 1.19	-23.31 ± 0.16	0.66	0.76	x	–	SD
Dust	–	-23.30 ± 0.19	0.79	0.94	x	–	SD
Tilted-ring	-6.68 ± 1.21	-23.26 ± 0.17	0.48	0.63	–	x	SD
Tilted-ring	–	-23.23 ± 0.23	0.65	0.86	–	x	SD
Tilted-ring	-8.07 ± 1.10	-23.05 ± 0.12	0.32	0.54	–	x	Inter
Tilted-ring	–	-23.03 ± 0.13	0.33	0.58	–	x	Inter
Hybrid	-8.38 ± 0.70	-23.12 ± 0.09	0.36	0.54	x	x	Inter+SD
Hybrid	–	-23.11 ± 0.09	0.37	0.57	x	x	Inter+SD

Notes. Column (1) describes the inclination method used to deproject the measured linewidth. Columns (2) and (3) show the best-fitting slope and zero-point, respectively, of the TFR of the form $M_{K_s} = a[\log_{10}(W_{20}/\text{km s}^{-1}) - 2.6] + b$, where Column (2) is blank the fit was constrained to have the same slope as that found by Tully & Pierce (2000), $a = -8.78$. Column (4) shows the intrinsic scatter (σ_{intr}) required by the fit to produce a reduced $\chi^2 \approx 1$. Column (5) shows the total rms scatter around the best-fitting relation. A cross in Column (6) denotes that the velocity widths used are from single-dish data, while a cross in Column (7) denotes that interferometric linewidths were used. Column (8) lists the selection method used to find galaxies that have gas beyond the peak of the circular velocity curve. ‘SD’ means that the galaxies’ single-dish profiles are boxy, while ‘Inter’ means that interferometric data were used to determine if the gas reaches beyond the peak of the circular velocity curve. The hybrid relations use both single-dish and interferometric data, as described in Section 2.6.1.

insufficient spatial resolution to strongly constrain the inclination of the molecular gas and this is reflected in the error bars. As can clearly be seen in this panel, the best-fitting relation is only marginally consistent with that of Williams et al. (2010). The intrinsic scatter of the best-fitting relation with a free and a constrained slope is 0.43 and 0.62 mag, with the total scatter of 0.60 and 0.82 mag, respectively.

The interferometric data, at least in some cases, allow us to further refine our technique for identifying galaxies that have reached beyond the peak of the circular velocity curve, by identifying nuclear rings and finding galaxies where a turnover can be seen in the position–velocity diagram. Interferometric observations are especially powerful in this regard, as the extent of the CO can be compared to the expected circular velocity curve from dynamical models. For example, NGC 7465, the obvious outlier in the previous plots, features a misaligned circumnuclear CO distribution, which has a double-horned profile, but has no turnover in its velocity field, and is extremely unlikely to reach beyond the peak of the galaxy rotation curve.

Aperture synthesis observations also allow us to identify cases where a galaxy is misclassified using the single-dish data because a pointing error and/or extended molecular gas results in only some smaller portion of the total velocity width being detected. Such cases include NGC 4324 and 4477 and PGC 58114. In a few cases where the profile shape was uncertain (due to low-signal-to-noise-ratio single-dish spectra), the interferometric data reveal that the gas does extend beyond the peak of the rotation curve, allowing us to include them. This is the case for NGC 3489 and 4292 and UGC 09519.

The TFR in the middle right-hand panel of Fig. 6 can thus be improved using the full knowledge gained from the interferometric data (discussed above) and this results in the TFR shown in the bottom left-hand panel of Fig. 6. The best-fitting TFR using this additional information agrees with that of Williams et al. (2010). The parameters of the best-fitting relations are again listed in Table 3. The intrinsic scatter of the best-fitting relation with a free and a constrained slope is 0.32 and 0.33 mag, with the total scatter of 0.54 and 0.58 mag, respectively.

4.1.4 Combining interferometric and single-dish data

Finally, we can combine our single-dish and interferometric observations, using the hybrid inclinations and velocities described in Section 2.6.1. These choices lead to the TFR shown in the bottom right-hand panel of Fig. 6. The parameters of the best-fitting TFRs are listed in Table 3. The best-fitting relations closely agree with the result of Williams et al. (2010), and the fits with a free and a constrained slope have an intrinsic scatter of 0.36 and 0.37 mag, with the total scatter of 0.54 and 0.57 mag, respectively. The intrinsic scatter found in this relation is similar to that found by a large study of the intrinsic scatter of the spiral galaxy TFR ($\sigma_{\text{intr}} \approx 0.4$ mag at bands between g and z ; Pizagno et al. 2007), and only very slightly larger than that found by Williams et al. (2010) ($\sigma_{\text{intr}} \approx 0.3$ mag at K_s band). The small total scatter reflects both the better number statistics and the use of the best possible measures of the rotation and inclination.

Using this hybrid relation, we can investigate if the residuals have any systematic behaviour with respect to the properties of the hosts. We find that the residuals are statistically uncorrelated with the galaxy K_s -band luminosity (Skrutskie et al. 2006), optical colour ($g - r$; Adelman-McCarthy et al. 2008; Scott et al., in preparation), velocity dispersion, galaxy total dynamical mass (Cappellari et al., in preparation) and spin parameter λ_R (Paper III).

5 DISCUSSION

5.1 CO as a tracer of galactic potentials

The results presented in Section 3.1 show that the CO emission accurately traces the potential of ETGs, if one has a suitable method of identifying which galaxies have extended molecular discs. Our work demonstrates that selecting galaxies via the profile shape is robust and does not systematically affect the measured rotation velocity. The main possible contaminant introduced by this selection is galaxies that have molecular rings, which would display a boxy profile without necessarily rotating at V_{flat} . Circumnuclear rings

pose the greatest problem, as they are very unlikely to rotate at V_{flat} , unlike inner and outer rings which are located at resonance points within the flat part of the galaxy circular velocity curve (e.g. Buta 1986). The number of galaxies with circumnuclear rings in our sample is likely to be small, as their presence in significant numbers would bias the best-fitting line in Fig. 3 to small values. This conclusion is also supported by the interferometric survey of Alatalo et al. (in preparation), which suggests that only a small percentage of local ETGs have their molecular gas restricted to the circumnuclear region.

One should also remember that the circular velocity curves of ETGs rise very quickly, normally peaking within one effective radius (e.g. Williams et al. 2009). This allows the molecular distribution to be compact, but still have enough gas beyond the peak of the galaxy circular velocity curve so that the linewidth is a good proxy of the circular velocity in that region. The good agreement between our derived TFR and that of Williams et al. (2010) suggests that the disc-halo conspiracy holds for our ETGs, at least out to $3R_c$. If this conspiracy holds even farther out into the dark matter dominated parts of these galaxies (which some authors suggest it does not, e.g. Dutton et al. 2010) will be considered in a future paper in this series.

5.2 Inclination measures

The problem of measuring the inclination of ETGs is not new, but it is complicated here as CO is often not aligned with the stars (e.g. Schinnerer & Scoville 2002; Young 2002; Crocker et al. 2008, 2009, 2011; Young et al. 2008), and it is the CO inclination that we require. As we have shown, methods using galaxy optical axial ratios are likely to yield large uncertainties and increase the scatter in the TFR, but they do not seem to significantly affect the determination of its slope or zero-point. This is likely because errors in the inclination are most problematic when the galaxy is close to face-on and the number of nearly face-on galaxies in our sample is small. The profile shape selection criterion also actively selects against face-on galaxies, where the velocity width is less than a few channel widths (no matter how extended the molecular gas is). In many H I TFR papers, galaxies with an inclination less than 45° are discarded (e.g. Tully & Fisher 1977), so this is not especially worrying. If we apply this cut in the inclination to our sample, then we retain within the errors the same TF slope and zero-point, and the rms scatter decreases. Even with a very harsh cut of 65° we retain the same relation. This demonstrates that our results are robust, and the slope and zero-point are minimally affected by the choice of the inclination correction.

As hinted above, while the slope and zero-point are robust, the scatter in the relation is affected by the inclination estimation method chosen. Moving from galaxy axial ratios to inclinations derived from dust features decreases the rms scatter around the best-fitting relation by ≈ 0.15 mag, if one removes the one obvious outlier. Our results do reveal a reduction in the total scatter when the inclinations are determined from fitting a thin disc model to interferometric data, despite our limited number statistics. With a larger sample one might expect the scatter to decrease further. In both cases, the decrease in the scatter is likely due to proper accounting for molecular gas distributions that do not rotate in the same plane as the stars. Unsurprisingly, to obtain the tightest relation, one must use measures of the inclination (such as unsharp-masked dust images or interferometric imaging of the molecular gas itself) that truly trace the inclination of the gaseous component.

5.3 Intrinsic scatter of the CO-TFR

The intrinsic scatter of our hybrid TFR is 0.36 mag, broadly consistent with typical values found in dedicated studies of the spiral galaxy TFR in the optical, such as those by Pizagno et al. (2007) (0.4 mag at the g and z bands) and Kannappan, Fabricant & Franx (2002) (0.4 mag at r band). Our intrinsic scatter is slightly larger than that found for S0 galaxies by Williams et al. (2010) (≈ 0.3 mag at K_s band). One reason for the increased scatter may be that Williams et al. (2010) considered S0 galaxies only, whereas our sample includes both morphologically classified E and S0 galaxies that span a wider range in λ_R , the stellar-specific angular momentum (Emsellem et al. 2007). This increased scatter may therefore be due to spanning an increased range in internal dynamics.

We do not have sufficient number statistics to constrain an E galaxy TFR separately, but the earliest-type galaxies (selected by the optical morphology) do lie on average to the faster and/or dimmer side of our relations. There is, however, no systematic behaviour within the residuals to the fit as a function of λ_R .

5.4 Offset from the spiral TFR

Exploring changes in the M/L of galaxies as a function of the morphological type is one of the main motivations for studying the early-type TFR. Williams et al. (2010) have highlighted the importance of comparing TFRs for each morphological type derived using the same tracer and methods, in order to minimize systematic differences. In this spirit, we use the spiral galaxy linewidths published by Chung et al. (2009), measured from on-the-fly mapping of 18 Virgo cluster members, in order to define a spiral CO-TFR.

We construct a TFR for the Chung et al. (2009) spirals in the same way as for our early-type sample, using 2MASS $K_{s,\text{total}}$ magnitudes and their W_{20} linewidths corrected for inclination. These inclinations were derived from the galaxy axial ratio and the morphological type using the classical Hubble formula from Hubble (1926). This formula effectively differs from equation (2.5.1) by making q_0 a function of the morphological type. For spiral galaxies such as those in the Chung et al. (2009) sample, this correction is small, corresponding to a q_0 less than 0.05, and hence this difference is unlikely to systematically affect the comparison of our results. We differ from Chung et al. (2009), however, by not assuming a set distance to the Virgo cluster, which has significant substructure. Instead, we use the distance to each galaxy as determined for the ATLAS^{3D} parent sample (Paper I). The resulting TFR is shown in Fig. 7. The values used to create this figure are listed in Table 4.

The best-fitting spiral TFR with an unconstrained gradient is

$$M_{K_s} = (-10.8 \pm 2.5) \left[\log_{10} \left(\frac{W_{20}}{\text{km s}^{-1}} \right) - 2.6 \right] - (24.1 \pm 0.2), \quad (5)$$

where the intrinsic scatter about the correlation is 0.68 mag, with the total scatter of 0.72 mag. The TFR obtained by constraining the fit to have the same slope as that of Tully & Pierce (2000) is

$$M_{K_s} = -8.78 \left[\log_{10} \left(\frac{W_{20}}{\text{km s}^{-1}} \right) - 2.6 \right] - (24.02 \pm 0.14), \quad (6)$$

with an intrinsic scatter of 0.55 mag and the total scatter of 0.59 mag.

Within observational errors, the best-fitting free and constrained spiral CO-TFRs are consistent with the relation of Tully & Pierce (2000). The offset between the unconstrained Chung et al. (2009) spiral CO-TFR and the hybrid early-type CO-TFR (discussed in

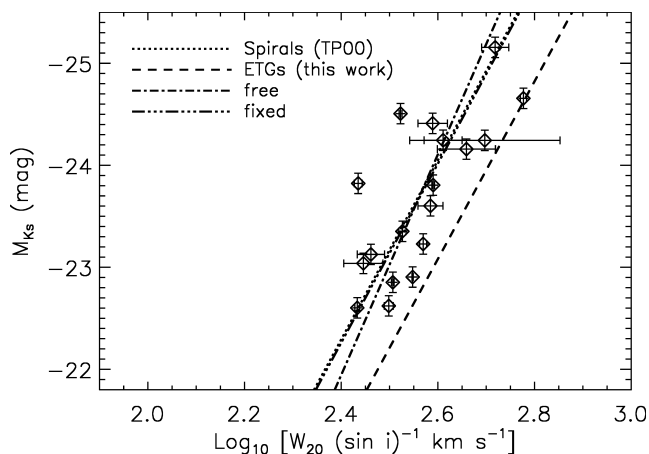


Figure 7. Spiral galaxy CO-TFR built in the same way as that shown in Fig. 6, but using W_{20} values and inclinations from the work of Chung et al. (2009).

Table 4. List of the parameters used to create the spiral TFR in Fig. 7.

Galaxy	Type	Distance (Mpc)	m_{K_s} (mag)	$i_{b/a}$ ($^\circ$)	W_{20} (km s^{-1})
(1)	(2)	(3)	(4)	(5)	(6)
NGC 4254	Sc	16.5	6.93	29 ± 7.3	221 ± 1
NGC 4298	Sc	16.5	8.47	59 ± 2.4	270 ± 4
NGC 4302	Sc	14	7.83	90 ± 0.1	353 ± 1
NGC 4303	Sc	16.5	6.84	$19 \pm 12.$	162 ± 2
NGC 4321	Sc	15.85	6.59	38 ± 5.2	239 ± 2
NGC 4402	Sc	16.5	8.49	80 ± 0.7	267 ± 3
NGC 4419	Sa	13.12	7.74	82 ± 0.6	318 ± 2
NGC 4438	Sb	16.5	7.27	87 ± 0.2	272 ± 5
NGC 4501	Sbc	15.3	6.27	60 ± 2.3	518 ± 2
NGC 4527	Sb	14.05	6.93	75 ± 1.1	376 ± 2
NGC 4535	Sc	15.75	7.38	41 ± 4.7	252 ± 5
NGC 4536	Sc	14.09	7.52	59 ± 2.4	318 ± 2
NGC 4548	Sb	18.71	7.12	35 ± 5.8	234 ± 6
NGC 4569	Sab	16.5	6.58	69 ± 1.6	311 ± 1
NGC 4579	Sab	21.3	6.49	39 ± 5.0	329 ± 1
NGC 4647	Sc	16.5	8.05	34 ± 6.0	156 ± 1
NGC 4654	Sc	16.5	7.74	58 ± 2.5	285 ± 1
NGC 4689	Sc	16.5	7.96	39 ± 5.0	182 ± 1

Notes. The galaxy sample listed in Column (1) comes from Chung et al. (2009). Column (2) lists the spiral galaxy type following the Hubble scheme (RC3; de Vaucouleurs et al. 1991). The distance to the galaxy in Column (3) is from the ATLAS^{3D} parent sample (Paper I). These distances are drawn preferentially from Mei et al. (2007) and Tonry et al. (2001). Column (4) lists the apparent K_s -band magnitudes taken from the 2MASS. Column (5) is the optical galaxy axial ratio, taken from the NED, as described in Section 2.5.1. The linewidths in Column (6) are taken directly from Chung et al. (2009).

Section 4.1.4) is 0.98 ± 0.22 mag, consistent within errors with the value found by Bedregal et al. (2006) and the offset found by Williams et al. (2010) between their S0 TFR and the Tully & Pierce (2000) relation.

This result is nevertheless surprising since Williams et al. (2010) argue that their offset with Tully & Pierce (2000) is flawed by systematic effects (the tracers and methods being different), and they prefer the much smaller offset (0.5 ± 0.14 mag) from their spiral galaxy sample treated identically to the S0s.

It is not immediately clear how our own result can be reconciled with this, as we use identical tracers and methods as Chung et al. (2009). However, we suspect that the different results are due to the mix of morphological types in the spiral samples. Williams et al. (2010) use a spiral sample consisting mostly of Sa–Sb spirals, while the sample of Chung et al. (2009) includes a larger fraction of later-type galaxies (mostly Sc), which are known to have a larger zero-point (e.g. Roberts 1978; Rubin et al. 1985; Masters, Springob & Huchra 2008; Shen et al. 2009). Classifying the Chung et al. (2009) sample more finely into morphological types does not necessarily support this explanation, however the number statistics are very limited.

5.5 Origin of the offset TFR for ETGs

In the ETG sample used in this paper, a few galaxies are consistent with the spiral galaxy relation and many lie between the spiral and early-type relations, consistent with the predictions of passive fading models (e.g. Dressler 1980; Dressler et al. 1997). The fact that the molecular gas is present in all these galaxies, however, suggests that many must have ongoing star formation (even if weak), and hence evolutionary models relying on a purely passive evolution are ruled out.

The presence of molecular gas mass fractions ranging from <0.1 to 5 per cent in these galaxies perhaps suggests an answer to some of the problems with passive evolution models. Bedregal et al. (2006) and Williams et al. (2010) both discuss the time-scale implied by the ETG–spiral TFR offsets observed, assuming passive fading, and find it uncomfortably short and inconsistent between the B and K_s bands. The presence of low levels of the residual star formation would prolong the period it takes for galaxies to fade and would contribute relatively more light at blue wavelengths than in the infrared. The molecular gas mass fraction in these galaxies is, however, small, so it is unclear if such a low mass fraction of young stars could extend the fading time-scale sufficiently.

An alternative explanation of the TFR offset is that the morphological (and luminosity) evolution is accompanied by a change in the size of the galaxies, affecting the galaxy rotation rather than its luminosity. Williams et al. (2010) suggest that a systematic contraction as spirals transform into S0s, consistent with the trend with the morphological type of the size–luminosity relation (Courteau et al. 2007), could explain the offset from the spiral TFR. Clearly, a combination of both effects is also possible.

5.6 High-mass end of the CO-TFR

As discussed in the Introduction, one motivation for studying the CO-TFR is the ability to probe the full mass range of galaxies, from small disc galaxies to large spheroids, with the same tracer and hence with the same assumptions and systematics. As an example of the power of this approach, we can investigate if our sample shows any evidence of a change in the slope of the TFR at the high-mass end, as reported by some authors (e.g. Peletier & Willner 1993; Verheijen 2001; Noordermeer & Verheijen 2007).

Our sample contains eight galaxies above the luminosity threshold suggested in previous works ($M_{K_s} \leq -23.75$). As can be seen in the bottom right-hand panel of Fig. 6, all but one of these systems are on, or to the right-hand side of, the best-fitting relation for the whole sample. When one compares the best-fitting TFR derived for the whole sample to that for just the fainter galaxies ($M_{K_s} \geq -23.75$), there is a small difference in the gradient and zero-point, in the direction found by other authors. We do not have

the number statistics to properly investigate the size of this effect, however, and hence only conclude that our results are consistent with the presence of a different slope at the high-mass end of the TFR.

5.7 Single-dish versus aperture synthesis

We have demonstrated in this work that single-dish spectra are sufficient to construct a robust CO-TFR and that galaxy inclinations can be taken from optical imaging without notably biasing its slope or zero-point (Section 5.2). However, one must exercise caution, as the small beams of millimetre telescopes can occasionally underestimate the linewidths of galaxies with extended molecular discs. Barring beam dilution effects, one would expect single-dish profiles to perform even better at higher redshifts, where the angular size of the target galaxies decreases. One caveat to this is that as the angular size of galaxies decreases, the source confusion may become a problem.

Naively, interferometric observations should be the best way to obtain an estimate of the true inclination of the molecular gas and hence reduce the artificial scatter in the TFR. Aperture synthesis observations also tend to have a large field of view and are thus less likely to face problems with extended gas distributions. Interferometric observations do, however, usually require a larger investment of the observing time per source. One must also choose the angular resolution of the data carefully, in order to avoid resolving out the most extended structures, while still having sufficient spatial information to constrain a tilted-ring model. Both single-dish and interferometric studies of the TFR should thus have a bright future.

6 CONCLUSIONS AND FUTURE PROSPECTS

In this paper, we have presented the first CO-TFR for ETGs. We have shown that CO linewidths are a reliable tracer of the circular velocity in fast-rotating ETGs and relations derived in this way agree well with ETG TFRs derived by other authors. We showed that our CO-TFR has a robust slope and zero-point, and a comparable scatter to that of TFRs derived with other techniques. The power of the CO-TFR is the ability to perform the same analysis easily for both spirals and ETGs (i.e. identical tracer and method), with purely observable quantities. This technique is therefore particularly suitable for comparing the morphological variations of the zero-point of the TFR.

The results presented in this paper show that ETGs follow a TFR that is offset by nearly 1 mag at the K_s band from that of spiral galaxies. This offset is similar to that found by previous authors. An offset ETG TFR is usually thought to be caused by the passive evolution of spiral galaxies into S0s, after an abrupt cessation of the star formation. However, the presence of the molecular gas in these ETGs suggests that the majority of this sample must have ongoing residual star formation, such as that revealed in a subsample of these galaxies (e.g. Temi, Brighenti & Mathews 2009; Crocker et al. 2011; Shapiro et al. 2010). This should increase the time-scale to fade by the required ≈ 1 mag. Some models, such as those that involve a change in the size of galaxies as they transform, do not require the star formation to cease completely, providing an alternative explanation that is fully consistent with our data. Unfortunately, the low molecular gas fractions in our systems make drawing any firm conclusions difficult.

Another area where the CO-TFR (for all spectral types) excels is the ability to extend the technique to higher redshifts, as discussed in Tutui et al. (2001). H I observations are currently limited to $z \lesssim$

0.2 (e.g. Catinella et al. 2008) and stellar kinematics to $z \lesssim 2$ (e.g. Cappellari et al. 2009; Cenarro & Trujillo 2009; van Dokkum, Kriek & Franx 2009), whereas CO has already been detected in galaxies at redshift $z > 6$ (e.g. Walter et al. 2004). The molecular content of galaxies is also expected to increase with the redshift, while the H I content stays approximately constant (Obreschkow & Rawlings 2009; Bauermeister, Blitz & Ma 2010; Daddi et al. 2010; Tacconi et al. 2010). CO velocity fields can be resolved and the rotation (and hence the dynamical mass) estimated even out to high redshift (e.g. Walter et al. 2004; Carilli et al. 2010). This raises the exciting prospect of being able to directly track the M/L evolution of galaxies as a function of both the redshift and morphological type, using an easily observable tracer (and without requiring dynamical modelling). New optical/infrared instrumentation is just starting to allow surveys of galaxy stellar kinematics out to $z \approx 2$ (e.g. Cappellari et al. 2009; Förster-Schreiber et al. 2009) and a comparison of these samples to linewidths derived with CO is a promising immediate avenue for future studies of the TFR.

Tutui et al. (2001) showed that constructing a (spiral galaxy) CO-TFR is already possible at up to redshift $z \sim 0.1$, but with the next generation of mm-wave telescopes due to enter service over the next few years, we should gain access to CO lines across the redshifted Universe for all morphological types. The Redshift Receiver System on the Large Millimeter Telescope, for instance, is optimized for the detection of redshifted transitions of the CO ladder from star-forming galaxies at cosmological distances and will generate a large data base of CO linewidths. If one is able to optically image these galaxies to estimate their inclination and morphology, then this will become an excellent resource for TFR analyses. With the ability to detect the spectral line emission from CO in a galaxy like the Milky Way at $z \sim 3$ in less than 24 h, the Atacama Large Millimeter Array (ALMA) will also be in an excellent position to study the CO-TFR at high redshift. The higher frequency bands that will be available at the ALMA also open up the possibility of detecting the [C II] emission (rest wavelength 158 μm), which is brighter than CO in many galaxies in the local Universe (Crawford et al. 1985) and possibly enhanced further at high redshift (Maiolino et al. 2009). [C II] may therefore become an important tracer of the circular velocity of high-redshift systems.

Although technical aspects will certainly be improved and the interpretation of this relation remains uncertain, we have shown that the ETG CO-TFR is a tantalizing and promising tool for galaxy evolution studies.

ACKNOWLEDGMENTS

TAD wishes to thank Gyula Jozsa for help and advice regarding the TiRiFiC package and Michael Williams for useful discussions and for providing his TFR fitting code. TAD and NS are supported by an STFC Postgraduate Studentship. MC acknowledges support from a STFC Advanced Fellowship (PP/D005574/1) and a Royal Society University Research Fellowship. This work was supported by the rolling grants ‘Astrophysics at Oxford’ PP/E001114/1 and ST/H002456/1 and visitor grants PPA/V/S/2002/00553, PP/E001564/1 and ST/H504862/1 from the UK Research Councils. RLD acknowledges travel and computer grants from Christ Church, Oxford, and the support from the Royal Society in the form of a Wolfson Merit Award 502011.K502/jd. RLD also acknowledges the support of the ESO Visitor Programme which funded a 3-month stay in 2010. RMMcD is supported by the Gemini Observatory, which is operated by the Association of Universities for Research in Astronomy, Inc., on behalf of the

international Gemini partnership of Argentina, Australia, Brazil, Canada, Chile, the United Kingdom and the United States of America. SK acknowledges support from the Royal Society Joint Projects Grant JP0869822. TN and MB acknowledge support from the DFG Cluster of Excellence ‘Origin and Structure of the Universe’. MS acknowledges support from a STFC Advanced Fellowship ST/F009186/1. The authors acknowledge financial support from the ESO. This paper is partly based on observations carried out with the IRAM 30-m telescope. The IRAM is supported by INSU/CNRS (France), MPG (Germany) and ING (Spain). Support for the CARMA construction was derived from the states of California, Illinois and Maryland, the James S. McDonnell Foundation, the Gordon and Betty Moore Foundation, the Kenneth T. and Eileen L. Norris Foundation, the University of Chicago, the Associates of the California Institute of Technology and the National Science Foundation. Ongoing CARMA development and operations are supported by the National Science Foundation under a cooperative agreement and by the CARMA partner universities. We acknowledge the use of the HyperLEDA data base (<http://leda.univ-lyon1.fr>) and the NED which is operated by the Jet Propulsion Laboratory, California Institute of Technology, under contract with the National Aeronautics and Space Administration. This publication makes use of data products from the 2MASS, which is a joint project of the University of Massachusetts and the Infrared Processing and Analysis Center/California Institute of Technology, funded by the National Aeronautics and Space Administration and the National Science Foundation.

REFERENCES

- Abazajian K. N. et al., 2009, *ApJS*, 182, 543
 Adelman-McCarthy J. K. et al., 2008, *ApJS*, 175, 297
 Bauermeister A., Blitz L., Ma C.-P., 2010, *ApJ*, 717, 323
 Bedregal A. G., Aragón-Salamanca A., Merrifield M. R., 2006, *MNRAS*, 373, 1125
 Bell E. F., de Jong R. S., 2001, *ApJ*, 550, 212
 Bertola F., Cinzano P., Corsini E. M., Rix H.-W., Zeilinger W. W., 1995, *ApJ*, 448, L13
 Bock D. C.-J. et al., 2006, in Stepp L. M., ed., *Proc. SPIE Vol. 6267, Ground-based and Airborne Telescopes*. SPIE, Bellingham, p. 13
 Buta R., 1986, *ApJS*, 61, 631
 Cappellari M., 2008, *MNRAS*, 390, 71
 Cappellari M. et al., 2006, *MNRAS*, 366, 1126
 Cappellari M. et al., 2009, *ApJ*, 704, L34
 Cappellari M. et al., 2010, *Highlights of Astronomy*, 15, 81
 Cappellari M. et al., 2011, *MNRAS*, 413, 813 (Paper I)
 Carilli C. L. et al., 2010, *ApJ*, 714, 1407
 Catinella B., Haynes M. P., Giovanelli R., Gardner J. P., Connolly A. J., 2008, *ApJ*, 685, L13
 Cenarro A. J., Trujillo I., 2009, *ApJ*, 696, L43
 Christodoulou D. M., Tohline J. E., Steiman-Cameron T. Y., 1988, *AJ*, 96, 1307
 Chung E. J., Rhee M.-H., Kim H., Yun M. S., Heyer M., Young J. S., 2009, *ApJS*, 184, 199
 Courteau S., Dutton A. A., van den Bosch F. C., MacArthur L. A., Dekel A., McIntosh D. H., Dale D. A., 2007, *ApJ*, 671, 203
 Crawford M. K., Genzel R., Townes C. H., Watson D. M., 1985, *ApJ*, 291, 755
 Crocker A. F., Bureau M., Young L. M., Combes F., 2008, *MNRAS*, 386, 1811
 Crocker A. F., Jeong H., Komugi S., Combes F., Bureau M., Young L. M., Yi S., 2009, *MNRAS*, 393, 1255
 Crocker A. F., Bureau M., Young L. M., Combes F., 2011, *MNRAS*, 410, 1197
 Daddi E. et al., 2010, *ApJ*, 713, 686
 de Vaucouleurs G., de Vaucouleurs A., Corwin H. G., Buta R. J., Paturel G., Fouque P., 1991, *Third Reference Catalogue of Bright Galaxies*. Springer-Verlag, New York
 de Zeeuw P. T. et al., 2002, *MNRAS*, 329, 513
 Dickey J. M., Kazes I., 1992, *ApJ*, 393, 530
 Dressler A., 1980, *ApJ*, 236, 351
 Dressler A. et al., 1997, *ApJ*, 490, 577
 Dutton A. A., Conroy C., van den Bosch F. C., Prada F., More S., 2010, *MNRAS*, 407, 2
 Emsellem E., Monnet G., Bacon R., 1994, *A&A*, 285, 723
 Emsellem E. et al., 2004, *MNRAS*, 352, 721
 Emsellem E. et al., 2007, *MNRAS*, 379, 401
 Emsellem E. et al., 2011, *MNRAS*, in press (arXiv:1102.4444, doi:10.1111/j.1365-2966.2011.18496.x) (Paper III)
 Faber S. M., Jackson R. E., 1976, *ApJ*, 204, 668
 Förster-Schreiber N. M., Genzel R., Bouché N., Cresci G., Davies R., Buschkamp P., Shapiro K., Tacconi L. J., 2009, *ApJ*, 706, 1364
 Gavazzi G., 1993, *ApJ*, 419, 469
 Gavazzi R., Treu T., Rhodes J. D., Koopmans L. V. E., Bolton A. S., Burles S., Massey R. J., Moustakas L. A., 2007, *ApJ*, 667, 176
 Gerhard O., Kronawitter A., Saglia R. P., Bender R., 2001, *AJ*, 121, 1936
 Ho L. C., 2007, *ApJ*, 669, 821
 Hubble E. P., 1926, *ApJ*, 64, 321
 Jarrett T. H., Chester T., Cutri R., Schneider S., Skrutskie M., Huchra J. P., 2000, *AJ*, 119, 2498
 Józsa G. I. G., Kenn F., Klein U., Oosterloo T. A., 2007, *A&A*, 468, 731
 Józsa G. I. G., Oosterloo T. A., Morganti R., Klein U., Erben T., 2009, *A&A*, 494, 489
 Kannappan S. J., Fabricant D. G., Franx M., 2002, *AJ*, 123, 2358
 Kent S. M., 1987, *AJ*, 93, 816
 Koribalski B., Dahlem M., Mebold U., Brinks E., 1993, *A&A*, 268, 14
 Krajnović D. et al., 2011, *MNRAS*, in press (arXiv:1102.3801, doi:10.1111/j.1365-2966.2011.18560.x) (Paper II)
 Kron R. G., 1980, *ApJS*, 43, 305
 Lavezzi T. E., 1997, PhD thesis, Univ. Minnesota
 Lavezzi T. E., Dickey J. M., 1997, *AJ*, 114, 2437
 Lavezzi T. E., Dickey J. M., 1998, *AJ*, 116, 2672
 Magorrian J., Ballantyne D., 2001, *MNRAS*, 322, 702
 Maiolino R., Caselli P., Nagao T., Walmsley M., Breuck C. D., Meneghetti M., 2009, *A&A*, 500, L1
 Markwardt C. B., 2009, in Bohlender D. A., Durand D., Dowler P., eds, *ASP Conf. Ser. Vol. 411, Astronomical Data Analysis Software and Systems XVIII*. Astron. Soc. Pac., San Francisco, p. 251
 Masters K. L., Springob C. M., Huchra J. P., 2008, *AJ*, 135, 1738
 Mei S. et al., 2007, *ApJ*, 655, 144
 Morganti R. et al., 2006, *MNRAS*, 371, 157
 Neistein E., Maoz D., Rix H.-W., Tonry J. L., 1999, *AJ*, 117, 2666
 Nilson P., 1973, *Acta Universitatis Upsaliensis. Nova Acta Regiae Societatis Scientiarum Upsaliensis – Uppsala Astronomiska Observatoriums Annaler*
 Noordermeer E., Verheijen M. A. W., 2007, *MNRAS*, 381, 1463
 Obreschkow D., Rawlings S., 2009, *ApJ*, 696, L129
 Okuda T., Kohno K., Iguchi S., Nakanishi K., 2005, *ApJ*, 620, 673
 Oosterloo T. A., Morganti R., Sadler E. M., van der Hulst T., Serra P., 2007, *A&A*, 465, 787
 Oosterloo T. et al., 2010, *MNRAS*, 409, 500
 Paturel G., Petit C., Prugniel P., Theureau G., Rousseau J., Brouty M., Dubois P., Cambréys L., 2003, *A&A*, 412, 45
 Peletier R. F., Willner S. P., 1993, *ApJ*, 418, 626
 Phillipps S., 1989, *A&A*, 211, 259
 Pizagno J. et al., 2007, *AJ*, 134, 945
 Rijke S. D., Zeilinger W. W., Hau G. K. T., Prugniel P., Dejonghe H., 2007, *ApJ*, 659, 1172
 Roberts M. S., 1978, *AJ*, 83, 1026
 Rogstad D. H., Lockhart I. A., Wright M. C. H., 1974, *ApJ*, 193, 309
 Rubin V. C., Burstein D., Ford W. K., Thonnard N., 1985, *ApJ*, 289, 81

- Sancisi R., 2004, in Ryder S. D., Pisano D. J., Walker M. A., Freeman K. C., eds, Proc. IAU Symp. 220, Dark Matter in Galaxies. Astron. Soc. Pac., San Francisco, p. 233
- Sault R. J., Teuben P. J., Wright M. C. H., 1995, in Shaw R. A., Payne H. E., Hayes J. J. E., eds, ASP Conf. Ser. Vol. 77, A Retrospective View of MIRIAD. Astron. Soc. Pac., San Francisco, p. 433
- Schinnerer E., Scoville N., 2002, ApJ, 577, L103
- Schoeniger F., Sofue Y., 1994, A&A, 283, 21
- Schoeniger F., Sofue Y., 1997, A&A, 323, 14
- Scott N. et al., 2009, MNRAS, 398, 1835
- Shapiro K. L. et al., 2010, MNRAS, 402, 2140
- Shen S., Wang C., Chang R., Shao Z., Hou J., Shu C., 2009, ApJ, 705, 1496
- Skrutskie M. F. et al., 2006, AJ, 131, 1163
- Sprayberry D., Bernstein G. M., Impey C. D., Bothun G. D., 1995, ApJ, 438, 72
- Steiman-Cameron T. Y., Kormendy J., Durisen R. H., 1992, AJ, 104, 1339
- Tacconi L. J. et al., 2010, Nat, 463, 781
- Temi P., Brighenti F., Mathews W. G., 2009, ApJ, 695, 1
- Tonry J. L., Dressler A., Blakeslee J. P., Ajhar E. A., Fletcher A. B., Luppino G. A., Metzger M. R., Moore C. B., 2001, ApJ, 546, 681
- Toribio M. C., Solanes J. M., 2009, AJ, 138, 1957
- Tully R. B., Fisher J. R., 1977, A&A, 54, 661
- Tully R. B., Fouque P., 1985, ApJS, 58, 67
- Tully R. B., Pierce M. J., 2000, ApJ, 533, 744
- Tutui Y., Sofue Y., 1997, A&A, 326, 915
- Tutui Y., Sofue Y., 1999, A&A, 351, 467
- Tutui Y., Sofue Y., Honma M., Ichikawa T., Wakamatsu K. I., 2001, PASJ, 53, 701
- van Dokkum P. G., Kriek M., Franx M., 2009, Nat, 460, 717
- Verheijen M. A. W., 2001, ApJ, 563, 694
- Walter F., Carilli C., Bertoldi F., Menten K., Cox P., Lo K. Y., Fan X., Strauss M. A., 2004, ApJ, 615, L17
- Weijmans A., Krajnović D., van de Ven G., Oosterloo T. A., Morganti R., de Zeeuw P. T., 2008, MNRAS, 383, 1343
- Williams M. J., Bureau M., Cappellari M., 2009, MNRAS, 400, 1665
- Williams M. J., Bureau M., Cappellari M., 2010, MNRAS, 409, 1330
- Wrobel J. M., Kenney J. D. P., 1992, ApJ, 399, 94
- Young L. M., 2002, AJ, 124, 788
- Young L. M., Bureau M., Cappellari M., 2008, ApJ, 676, 317
- Young L. M. et al., 2011, MNRAS, in press (arXiv:1102.4633, doi:10.1111/j.1365-2966.2011.18561.x) (Paper IV)
- Zwaan M. A., van der Hulst J. M., de Blok W. J. G., McGaugh S. S., 1995, MNRAS, 273, L35

This paper has been typeset from a $\text{\TeX}/\text{\LaTeX}$ file prepared by the author.